Volume 27
Number 42
14 November 2025
Pages 6839–6968

CrystEngComm

rsc.li/crystengcomm

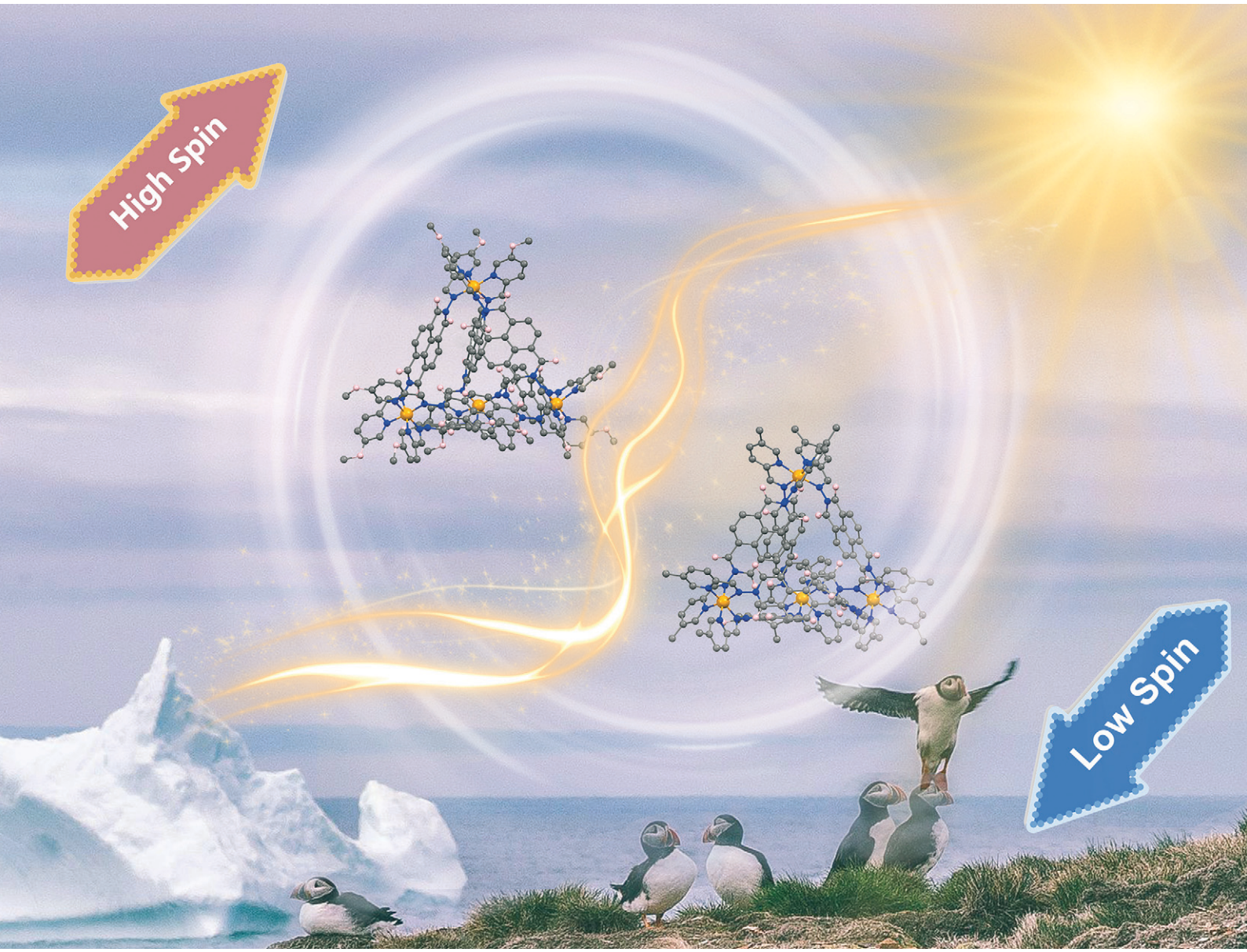

ISSN 1466-8033

ROYAL SOCIETY OF CHEMISTRY

HIGHLIGHT

Yann Garcia *et al.*

Recent advances in spin crossover Fe(II) tetrahedral metal–organic cages and their solid-state applications

CrystEngComm

ROYAL SOCIETY OF CHEMISTRY

HIGHLIGHT

View Article Online
View Journal | View Issue

Cite this: *CrystEngComm*, 2025, **27**, 6848

Recent advances in spin crossover Fe(II) tetrahedral metal–organic cages and their solid-state applications

Weiyang Li,[ab] Xiaochun Li,[b] Mengmeng Wang,[b] Yanfeng Bi [a] and Yann Garcia *[b]

Received 4th July 2025,
Accepted 3rd September 2025

DOI: 10.1039/d5ce00671f

rsc.li/crystengcomm

Tetrahedral Fe(II)-based metal–organic cages represent a distinctive family of spin crossover materials that display tunable magnetic bistability in the solid state under thermal, chemical or photonic stimuli. This review summarizes the latest progress in the design, synthesis and characterization of such Fe(II) spin crossover cages, with particular emphasis on how ligand field strength, host–guest interactions, and intermolecular interactions influence their spin-state switching behavior and spin-state distribution. Representative cage architectures, including face-capped $Fe(II)_4L_4$ and edge-bridged $Fe(II)_4L_6$ systems, are discussed in detail, focusing on their structural features and spin crossover properties as elucidated by single-crystal X-ray diffraction, magnetic susceptibility measurements and ^{57}Fe Mössbauer spectroscopy. In addition, we highlight emerging solid-state applications of these spin crossover cages, such as gas sensing and guest-responsive adsorption. Finally, we outline main hurdles and future research directions for the development of tetrahedral Fe(II) based spin crossover cages as functional molecular materials.

1. Introduction

Spin crossover (SCO) in transition metal complexes with $3d^4$–$3d^7$ electron configurations has attracted considerable attention due to its relevance to potential applications in memory storage, molecular electronics, spintronic devices, and chemical sensing.[1–7] This phenomenon arises from the reversible switching between high-spin (HS) and low-spin (LS) states, which can be triggered by various external stimuli such as changes in temperature, pressure, electric fields, light irradiation, or guest binding (Fig. 1).[8–16] In 1963, Madeja and König reported the first Fe(II) SCO compound $[Fe(phen)_2X_2]$ (phen = 1,10-phenanthroline) and studied the anion effects on the spin state.[17] This work provided a solid foundation for the study of Fe(II) SCO compounds. To date, Fe(II) containing compounds remain the most widely investigated SCO systems, characterized by significant magnetic, structural and optical variations upon spin-state switching.[4,18–23]

SCO systems were previously recognized as potential molecular switches in memory storage devices from a materials standpoint.[12,24–27] In general, desirable SCO properties typically include complete and abrupt transitions, thermal hysteresis and room temperature switchability. Such behaviors are governed not only by the intrinsic ligand field strength and structural features of the complex, but also by the degree of cooperativity, which arises from both intra- and intermolecular interactions.[7,28–33] Strong interactions between Fe(II) centers are typically present in systems with high cooperativity, allowing for this "communication" to take place.[34–36] Covalently connecting numerous metal centers in a polynuclear or polymeric architecture can potentially impart cooperativity, however it should be emphasized that this method is not necessarily guaranteed to work.[36] A successful case is the 1,2,4-triazole polymers studied by Kahn and co-workers.[37–42] Comparable to polymeric systems, discrete polynuclear complexes have the benefit of more controllable design and synthesis as well as simpler characterization.[36,43] For example, the crystal structure of the extensively studied $[Fe(Rtrz)_3]^{2+}$ (R = 4-amino-1,2,4-triazole) chains was only obtained in 2011.[44] Therefore, increasing research interest has focused on polynuclear Fe(II) SCO systems, particularly tetrahedral cages, whose intrinsic

Fig. 1 Schematic illustration of the d orbital splitting in an octahedral Fe(II) ion. External stimuli such as temperature, pressure, light, magnetic or electric fields and guest binding can induce spin-state switching.

[a] *School of Petrochemical Engineering, Liaoning Petrochemical University, Fushun 113001, P.R. China*
[b] *Institute of Condensed Matter and Nanosciences, Molecular Chemistry, Materials and Catalysis (IMCN/MOST), Université catholique de Louvain, Place Louis Pasteur 1, 1348 Louvain-la-Neuve, Belgium. E-mail: yann.garcia@uclouvain.be*

cavities enable the tuning of SCO properties *via* guest inclusion.[45–50] In addition to the confined guests inside the cavities, guest molecules located in the lattice between cages can also critically influence spin-state switching. Thus, both types of host–guest interactions play a decisive role in modulating SCO behavior, and the associated spin-state transitions are often accompanied by distinct optical responses, providing opportunities for the development of SCO cages as colorimetric sensors.[51–53] Furthermore, molecular storage applications typically require systems with at least two stable spin states. Fe(II) based SCO cages, in principle, can access up to five distinct spin configurations, *i.e.*, $(Fe^{II}LS)_n(Fe^{II}HS)_{4-n}$ (n = 0–4), offering enhanced potential for multi-state data storage.[43] Although higher-nucleated supramolecular complexes such as Fe_6 supramolecular nanoballs and Fe_8 cubes[36,54–60] may have similar or even superior magnetic properties to tetranuclear cages, the relative complexity of their ligand design, synthesis, and characterization methods has led to even more sparse research in this area.[36]

There are two configurations for Fe(II) tetrahedral cages, the edge-bridged Fe_4L_6 (Fig. 2a)[61] and the face-caped Fe_4L_4 (Fig. 2b),[62] constructed from six bis-bidentate ligands located at the edges of the tetrahedron and four tritopic bidentate ligands located on the faces of the tetrahedron, respectively.[63–66] Regarding the synthesis of Fe(II) cages, subcomponent self-assembly methods with simple synthesis and analytical procedures have been widely used. This method generates complicated structures from simple building blocks through the simultaneous formation of dynamic (N=C) bonds and coordinative (N→Fe) linkages.[48,67–70] A large number of Fe(II) tetrahedral cages reported to date, particularly those assembled through subcomponent self-assembly, exhibit LS states due to the strong ligand fields imposed by pyridine-imine and 2,2′-bipyridyl-based donors.[61,62,71,72]

Compared to pyridine nitrogen atoms, imidazole nitrogen donors generally generate a weaker ligand field. As a result, imidazole–imine coordination environments may offer an appropriate ligand field strength to support SCO behavior in Fe(II) cage complexes.[73–75] On this basis, in 2013, the Kruger group reported the first SCO cage adopting a face-capped configuration, in which imidazole–imine coordination sites played a key role in achieving spin state conversion.[76] In Fig. 3, all the ligands used for the construction of Fe(II) SCO tetranuclear cages are summarized.[53,76–87] In addition, as the bond length between the metals (Fe–Fe distance) and the volume of the cavity are two other key parameters for cage-like compounds, we have summarized and compared them as well (Table 1). In this review, we provide an overview of Fe(II)-based SCO tetrahedral cages, with particular emphasis on their behavior in the solid state. We outline strategies for ligand design and cage construction, and summarize representative structural types including face-capped and edge-bridged configurations reported to exhibit SCO. Special attention is given to how subtle changes in ligand field strength, intermolecular interactions and host–guest interactions influence the solid-state spin-state switching properties. In addition, we highlight recent advances in the development of SCO cages as functional materials for solid-state applications.

The cavity volumes were calculated by MoloVol:[88] large probe radius in Å = 3; spatial resolution of the underlying grid in Å = 0.5. The rest of calculations were done with default values of 1.2 Å and 0.2 Å, respectively. It is worth noting that the cavity volumes we studied are generally confined, *i.e.*, unlinked to the outside of the cage. So unclosed cavity volumes are not considered in this table.

2. Fe_4L_4 type SCO cages and their application

Kruger *et al.* reported the first example of a face-capped tetrahedral SCO cage, termed as cage **1**.[76] This discrete tetrahedral cage was synthesized *via* subcomponent self-assembly by reacting $Fe(BF_4)_2{\cdot}6H_2O$ with 2,4,6-tris(4-aminophenoxy)-1,3,5-triazine and 2-imidazolecarboxaldehyde in acetonitrile (Fig. 4a). The C_3-symmetric ligands are

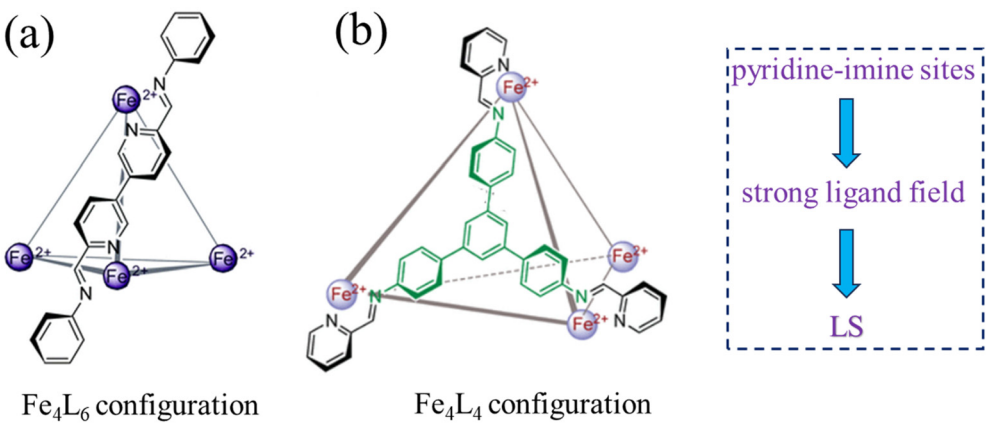

Fig. 2 Representation of two typical LS cages based on pyridine–imine building blocks with edge-bridged Fe_4L_6 (a)[61] and face-caped Fe_4L_4 (b)[62] configurations.

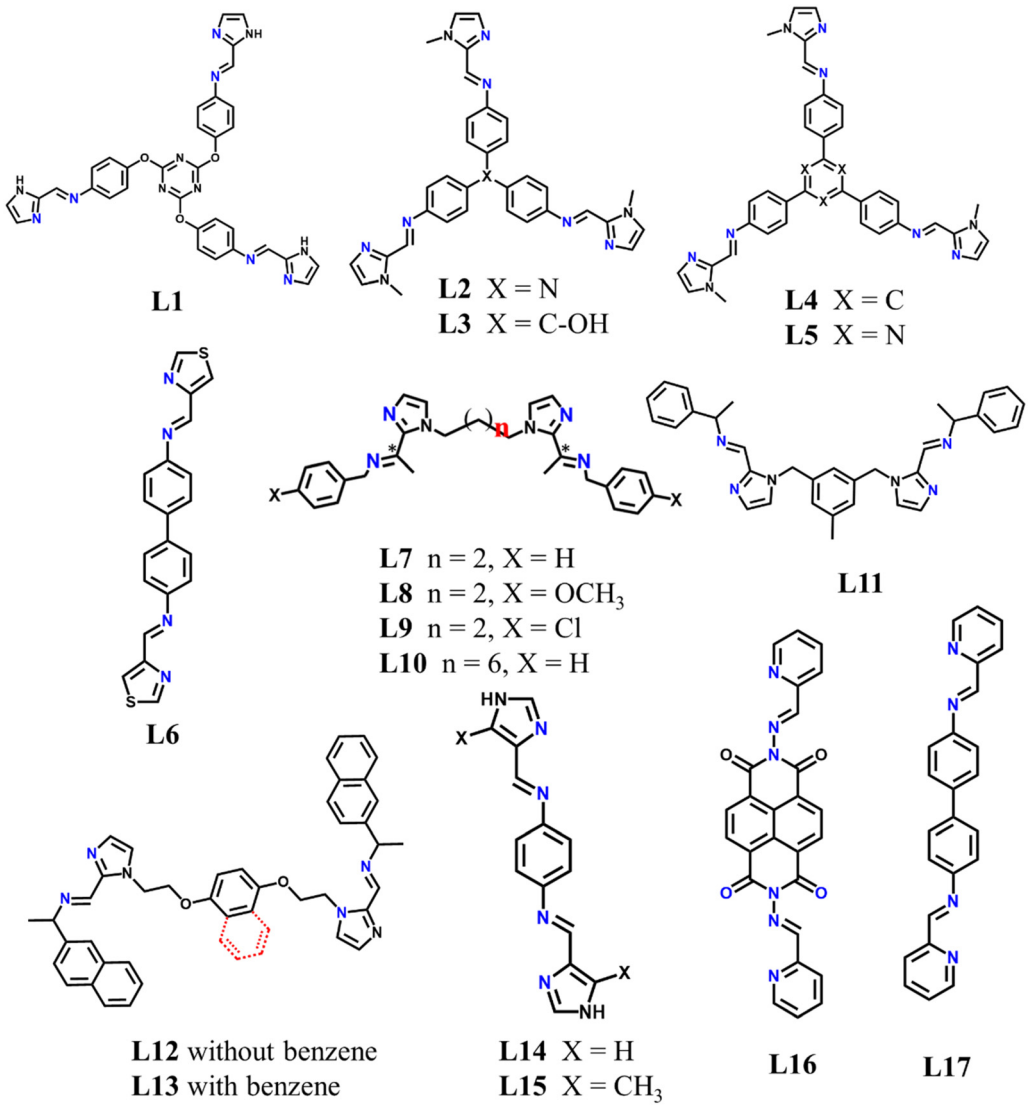

Fig. 3 Ligand structures used to prepare SCO Fe_4L_4 (**L1**–**L5**) and Fe_4L_6 (**L6**–**L17**) cages. For **L7**–**L9**, both the (*R*,*R*) and (*S*,*S*) structures at the chiral (*) center were employed to build coordination complexes.

located at the faces of the tetrahedron, while the four Fe(II) centers occupy the vertices (Fig. 4b). A single BF_4^- anion is encapsulated within the cavity, while the remaining BF_4^- ions reside outside the cage, participating in hydrogen bonding with imidazole N–H groups to form a 3D hydrogen-bonded network. Variable-temperature magnetic susceptibility measurements were employed to study the SCO behaviours (Fig. 4c). The $\chi_m T$ value at 290 K is 7.4 cm^3 K mol^{-1}, indicating a partially populated HS state (around 60% HS). Upon cooling, the value gradually decreases, reaching ~0.15 cm^3 K mol^{-1} at 60 K, consistent with complete transition to the LS state. Fitting the magnetic data with the ideal solution model gave thermodynamic parameters of ΔH = 14.1 kJ mol^{-1} and ΔS = 50.3 J K^{-1} mol^{-1} with a transition temperature $T_{1/2}$ = 284 K. Single crystal X-ray diffraction (SXRD) studies at variable temperatures revealed a 7.5% increase in the cage cavity volume upon SCO, accompanied by elongation of Fe–N bond distances and expansion of the unit cell, further supporting the spin-state transition. In addition, photoinduced spin-state switching was observed at 10 K under white-light irradiation (2 mW cm^{-2}), where the $\chi_m T$ value increased from 0.13 to 0.46 cm^3 K mol^{-1} after prolonged exposure. The metastable HS state relaxes thermally around 60 K, suggesting the photoinduced effect is localized near the surface and limited in extent. As the first example of a Fe(II) SCO cage, this work not only demonstrated the feasibility of integrating SCO behavior into a well-defined cage architecture, but also established the imidazole–imine coordination strategy as a key platform for the development of subsequent SCO active molecular cages.

In the same year, Nitschke, Brooker and co-workers reported two new $Fe(II)_4L_4$ type cages synthesized by subcomponent self-assembly using 2-formyl-*N*-methylimidazole and triamines A or B, yielding cages **2** and **3**, respectively (Fig. 5a).[77] Both structures feature

Table 1 Structural information and SCO properties for representative Fe(II) tetrahedral cages

Cage	Temperature (K)	Fe–Fe distance$_{av}$ (Å)	Cavity volume (Å^3)	SCO behaviour	CCDC number	Ref.
$[Fe_4(L1)_4](BF_4)_8{\cdot}14.75MeCN{\cdot}4.5C_6H_6{\cdot}3H_2O$, **1**	153	14.16	108.84	Gradual	907705	76
$[Fe_4(L1)_4](BF_4)_8{\cdot}14.75MeCN{\cdot}4.5C_6H_6{\cdot}3H_2O$, **1**	293	14.33	112.30	Gradual	907706	76
$[Fe_4(L3)_4](CF_3SO_3)_8$, **2**	100	11.85	57.05	Gradual	908546	77
$[Fe_4(L4)_4](BF_4)_4{\cdot}16MeCN$, **4**	100	14.76	202.09	Gradual	1057843	78
$[Fe_4(L5)_4](BF_4)_4$ + solvent, **5**	100	14.59	BF_4^- included	Gradual	2157667	53
$[Fe_4(L7)_6](ClO_4)_8$ (R), **6**	150	9.62	85.02	Gradual	1025013	79
$[Fe_4(L7)_6](ClO_4)_8$ (S), **6**	123	9.57	81.07	Gradual	1025014	79
$[Fe_4(L8)_6](ClO_4)_8{\cdot}11.59MeCN{\cdot}2C_4H_{10}O{\cdot}H_2O$ (R), **7**	123	9.64	85.42	Gradual	1025015	79
$[Fe_4(L8)_6](ClO_4)_8{\cdot}6MeCN$ (S), **7**	123	9.68	89.73	Gradual	1025016	79
$[Fe_4(L9)_6](ClO_4)_8{\cdot}2MeCN$ (S), **8**	123	9.67	90.46	Gradual	1025017	79
$[Fe_4(L10)_6](BF_4)_8$, **9**	173	11.38	1D channel	Gradual	1447306	80
$[Fe_4(L6)_6](BF_4)_8$ + solvent, **10**	100	12.75	78.13*	Gradual, $T_{1/2\downarrow}$ = 311 K, $T_{1/2}{}^{\uparrow}$ = 340 K, 29 K hysteresis	1914986	81
$[Fe_4(L11)_6](ClO_4)_8$, **11**	173	9.59	83.98	Gradual	1873319	82
$[Fe_4(L12)_6](CF_3SO_3)_8$ + solvent, **12**	173	12.38	Cube-like cavities	Gradual, $T_{1/2}$ = 344 K	1847958	83
$[Fe_4(L13)_6](CF_3SO_3)_8$ + solvent, **13**	173	12.23	Cube-like cavities	Gradual, $T_{1/2}$ = 328 K	1847959	83
$[Fe_4(L14)_6](ClO_4)_8{\cdot}10MeNO_2{\cdot}5.6H_2O$, **14**	113	8.68	0	Gradual	1959705	84
$[Fe_4(L15)_6](BF_4)_8{\cdot}10.8MeCN{\cdot}4H_2O$, **15**	113	8.73	0	Gradual	1959706	84
$[Fe_4(L16)_6](BF_4)_8{\cdot}3.64(C_4H_8O){\cdot}2(C_2H_3N)$ + solvent, **16**	120	12.71	0	Gradual	2191810	85
$[Fe_4(L16)_6](ClO_4)_8{\cdot}3(C_2H_3N)$ + solvent, **17**	120	12.63	0	Gradual	2270896	86
$[Fe_4(L16)_6](CF_3SO_3)_{13}{\cdot}11(C_2H_3N)$ + solvent, **18**	100	12.29	0	Gradual	2270897	86

tris(iminoimidazole) ligands coordinated to Fe(II) centers (Fig. 5b). In the solid state, cage **2** exhibits a gradual SCO transition from a HS state at 298 K (χ_mT = 12.99 cm^3 K mol^{-1}) to a predominantly LS state at 50 K (χ_mT = 4.61 cm^3 K mol^{-1}), corresponding to approximately 75% conversion (Fig. 5c). Variable-temperature Mössbauer spectroscopy further confirmed the coexistence of spin states and the SCO process, showing characteristic changes in isomer shift (δ) and quadrupole splitting (ΔE_Q) consistent with the transition from HS to LS Fe(II) centers (Fig. 5d). In contrast, cage **3**, which contains a more pyramidal triamine on the ligand structure, remains LS at room temperature and undergoes guest-responsive SCO in solution. Variable-temperature ^{1}H NMR spectroscopy in nitromethane revealed a gradual spin-state conversion ($T_{1/2}$ = 333 K), which is subtly modulated by guest encapsulation: the presence of CS_2 or Br^- within the cavity lowers the transition temperatures $T_{1/2}$ to 324 K and 328 K, respectively. Furthermore, this study demonstrated that even small modifications to the ligand structure, such as changes in the geometry of the triamine component, can result in dramatic differences in the solid-state magnetic properties of the resulting cage, highlighting the sensitivity of SCO behavior to structural perturbations.

In 2015, Li *et al.* reported a large tetrahedral $Fe(II)_4L_4$ cage, termed as cage **4**, constructed *via* metal-directed self-assembly using a rigid, C_3-symmetric tris-bidentate ligand bearing imidazole–imine coordination sites.[78] SXRD analysis revealed a *T*-symmetric tetrahedron with Fe–Fe distances ranging from 14.5 to 15.1 Å (Fig. 6a). Magnetic susceptibility measurements demonstrated a gradual and incomplete SCO transition from 300 K to 50 K. For the solvated form (Fig. 6b), the χ_mT value declined from 11.44 cm^3 K mol^{-1} at 300 K to 7.85 cm^3 K mol^{-1} at 50 K, while the desolvated sample showed a larger drop from 11.60 cm^3 K mol^{-1} at 400 K to 8.29 cm^3 K mol^{-1} at 50 K, indicating approximately 30% conversion to the LS state (Fig. 6c). Mössbauer spectroscopy at 5 K revealed two distinct doublets corresponding to HS (δ = 1.26 mm s^{-1}, ΔE_Q = 2.18 mm s^{-1}) and LS (δ = 0.21 mm s^{-1}, ΔE_Q = 0.94 mm s^{-1}) Fe(II) species in a 67% : 33% ratio, consistent with magnetic data and suggesting that only one of the four metal centers undergoes SCO (Fig. 6d). Notably, irradiation with a λ = 532 nm laser at 5 K induced a significant increase in χ_mT value, clearly demonstrating a light induced excited spin state trapping (LIESST) effect.

On this basis, by introducing subtle modification to the ligand structure, *i.e.*, by replacing the central core with a more electron-deficient triazine unit while maintaining the imidazole–imine coordination motif, Garcia and co-workers constructed a new SCO $Fe(II)_4L_4$ cage (**5**), which operates as a rapid colorimetric sensor for gaseous ammonia under ambient conditions.[53] The cage was assembled *via* subcomponent self-assembly from $Fe(BF_4)_2{\cdot}6H_2O$, 2,4,6-tris(4-aminophenyl)-1,3,5-triazine, and 1-methyl-2-imidazolecarboxaldehyde in a 4 : 4 : 12 stoichiometric ratio in acetonitrile (Fig. 7a). SXRD at 100 K revealed that the cage adopts a tetrahedral geometry (Fig. 7b). Each Fe(II) center adopts a distorted octahedral FeN_6 coordination environment and one BF_4^- anion is encapsulated in the cage cavity. Cage **5** exhibits a rapid and distinct color change from light brown to purple upon exposure to $NH_{3(g)}$

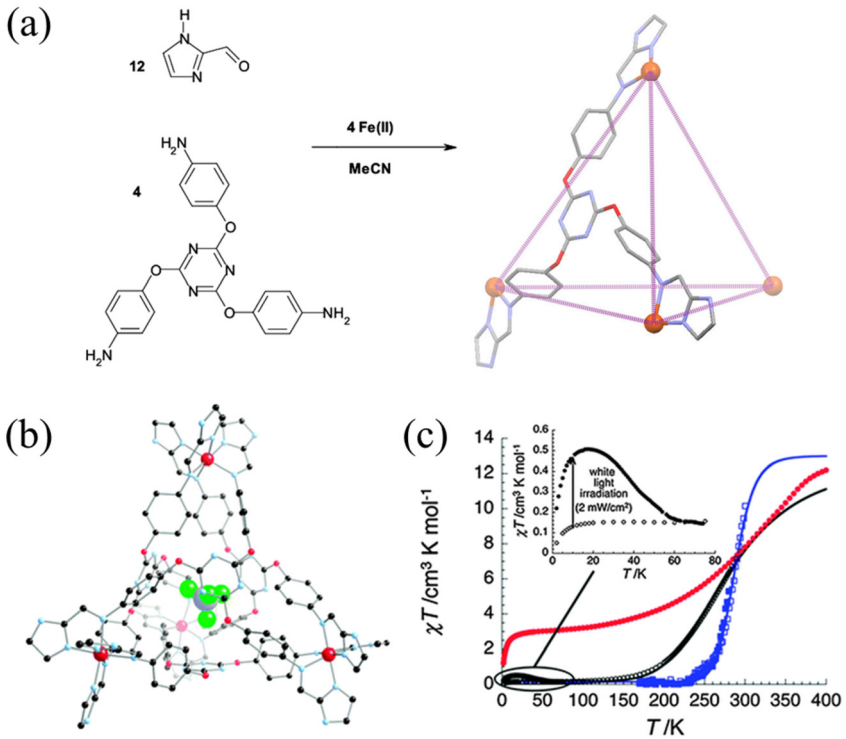

Fig. 4 Synthesis method (a) and crystal structure of **1** (b). (c) $\chi_m T$ *vs.* *T* plots for the solvated **1** (black), dried **1** (red) and in solution (blue).[76]

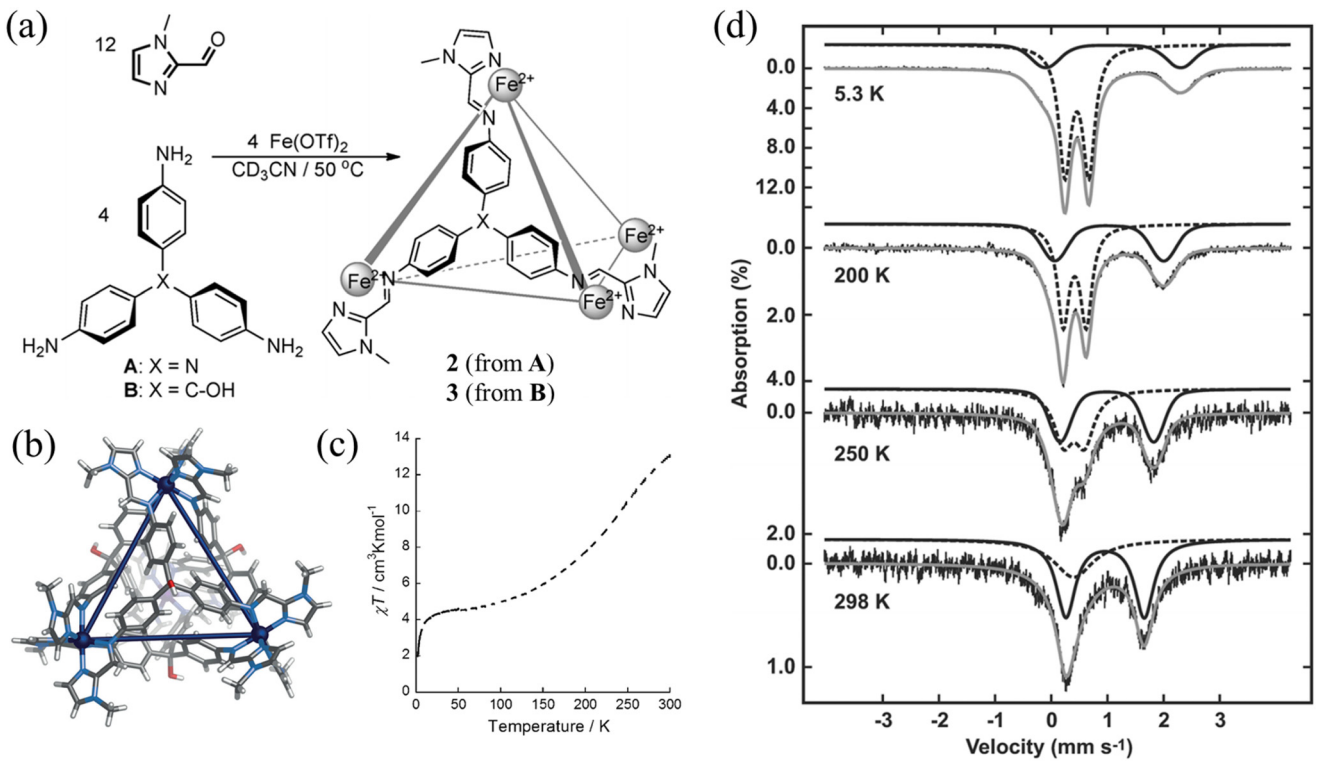

Fig. 5 (a) Synthesis method of cages **2** and **3**. (b) Crystal structure of cage **2**. $\chi_m T$ *vs.* *T* plots (c) and variable-temperature ^{57}Fe Mössbauer spectra (d) for cage **2**. Adapted from ref. 77.

at room temperature, occurring within 10 s (Fig. 7c). Diffuse reflectance spectroscopy and ^{57}Fe Mössbauer analysis confirmed that $NH_{3(g)}$ adsorption induces a spin-state transition from HS to LS at the Fe(II) centers (Fig. 7c). In

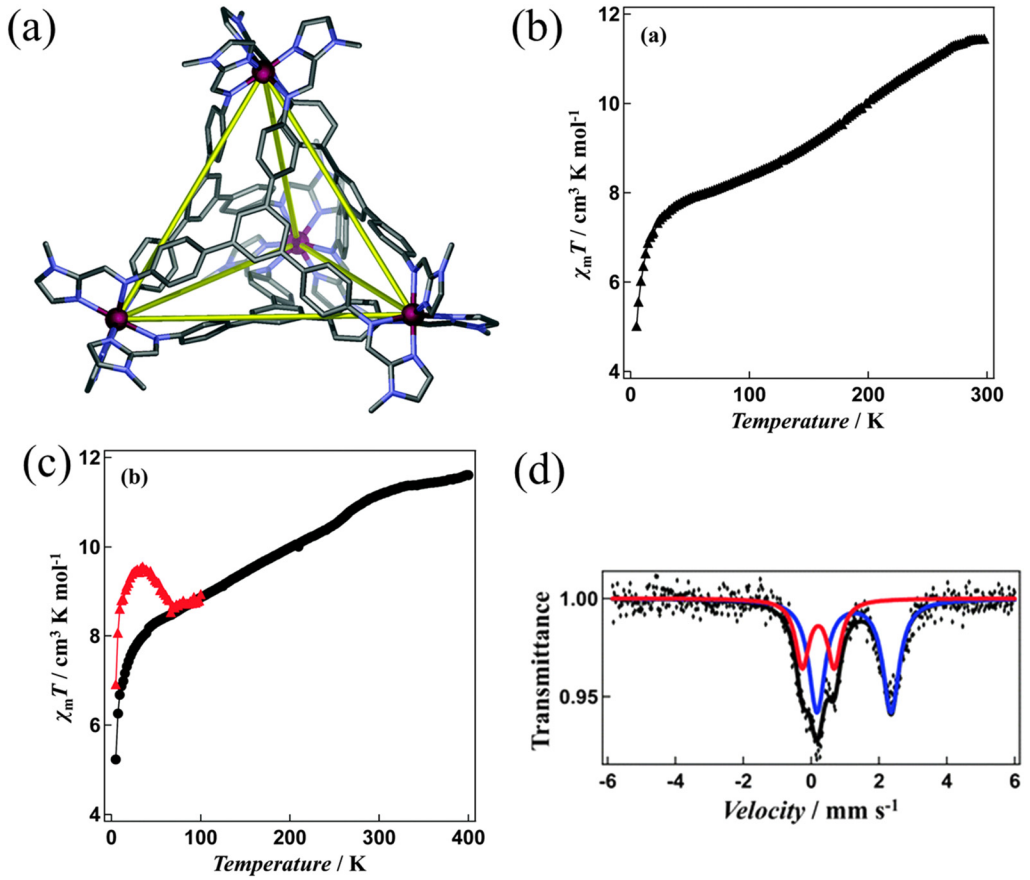

Fig. 6 (a) Crystal structure of cage **4**. $\chi_m T$ *vs.* *T* plots for solvated (b) and non-solvated (c) cage complexes. ^{57}Fe Mössbauer spectrum for cage **4** recorded at 5 K (d).[78]

the pristine state at 298 K, Mössbauer spectroscopy revealed a mixed-spin state population, with three quadrupole doublets corresponding to LS Fe(II) (δ = 0.20 mm s^{-1}, ΔE_Q = 0.70 mm s^{-1}, *A* = 29%) and two HS Fe(II) species (HS-1: δ = 0.99 mm s^{-1}, ΔE_Q = 1.39 mm s^{-1}, *A* = 44%; HS-2: δ = 1.10 mm s^{-1}, ΔE_Q = 2.60 mm s^{-1}, *A* = 27%) (Fig. 7e). Upon $NH_{3(g)}$ exposure, the LS : HS ratio increased to 60%:40%, indicating a significant spin-state conversion (Fig. 7f). This guest-induced SCO is attributed to hydrogen bonding and electronic interactions between NH_3 molecules and the N-rich ligand framework, which perturbs the ligand field and favor stabilization of the LS state. SQUID magnetometry further supported the sensing mechanism, showing a marked decrease in the $\chi_m T$ value at 298 K, *i.e.*, from 11.92 cm^3 K mol^{-1} in the pristine sample to 8.43 cm^3 K mol^{-1} after $NH_{3(g)}$ treatment, proving the increase in LS population (Fig. 7d). Moreover, cage **5** was successfully applied as a visual indicator for real-time pork spoilage monitoring at 4 °C, *i.e.* in fridge storage conditions, correlating $NH_{3(g)}$ release with food degradation, as a result of the development in bacteria in meat samples. Therefore, SCO cage **5** exhibits excellent optical responsiveness, making it a promising candidate for practical ammonia sensing and smart packaging applications.[53]

3. Fe_4L_6 type SCO cages and their application

In 2015, Gu *et al.* reported a family of enantiopure $Fe(II)_4L_6$ cages synthesized *via* highly diastereoselective subcomponent self-assembly from 1,4-di(imidazole-2-carboxaldehyde)butane, chiral phenylethylamines, and $Fe(ClO_4)_2{\cdot}6H_2O$ (Fig. 8a).[79] The resulting cages (**6–8**) adopt *T*-symmetric tetrahedral architectures, in which four Fe(II) centers occupy the vertices and six C_2-symmetric imidazole–imine ligands define the edges. Each Fe(II) center is coordinated in a fac-Δ or fac-Λ geometry depending on the absolute configuration of the chiral amine, resulting in homochiral ΔΔΔΔ or ΛΛΛΛ cage enantiomers (Fig. 8b). SXRD confirmed the chiral structures and revealed Fe–Fe distances of 9.41–9.81 Å and Fe–N bond lengths of 1.916–2.06 Å, consistent with LS Fe(II). Magnetic susceptibility measurements revealed gradual and incomplete SCO transitions near room temperature. Upon heating from 2 K to 400 K, the $\chi_m T$ values increased from ~0.1–1.0 cm^3 K mol^{-1} to a maximum of 8.84–10.49 cm^3 K mol^{-1} for cages **6–8**, indicating a partial conversion to the HS state (73.7–87.4%) (Fig. 8c). The SCO behavior was strongly influenced by ligand substituents and solvent content. Thermal desolvation led to decreased spin-state populations and more

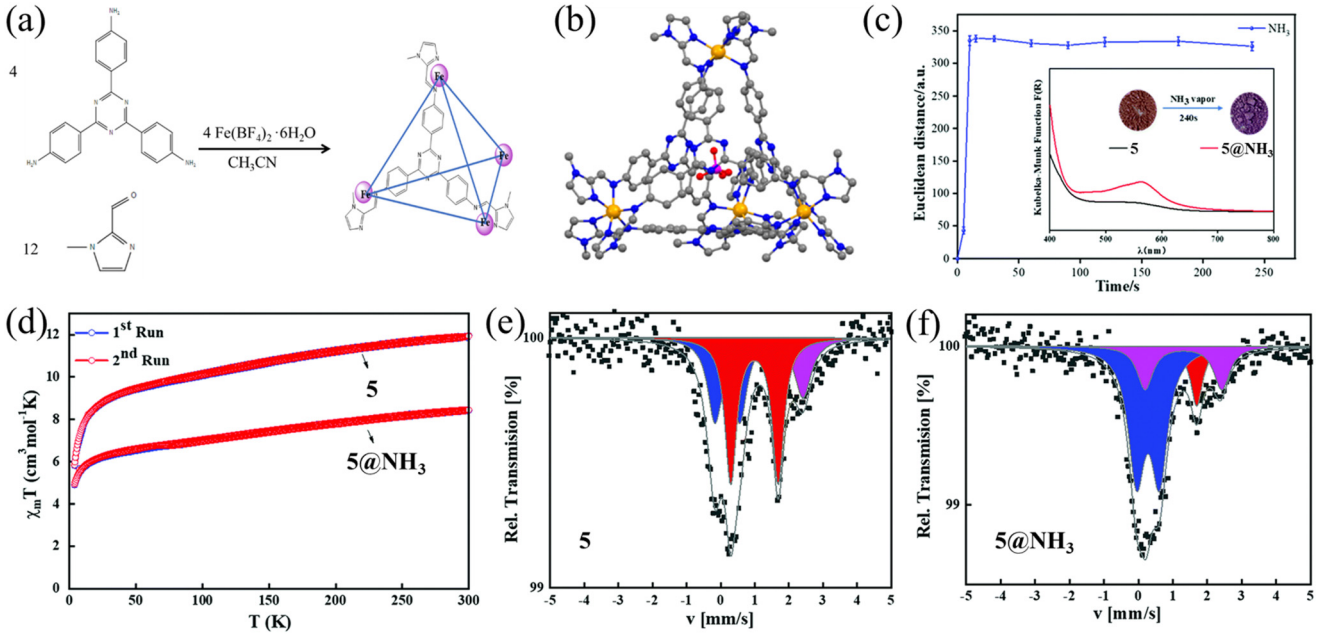

Fig. 7 Synthesis method (a) and crystal structure (b) of **5**. (c) Response time of **5** to $NH_{3(g)}$ at room temperature. Inset: diffuse reflectance spectroscopy and photos of **5** and **5**@$NH_{3(g)}$. χ_mT *vs.* *T* plots (d) and ^{57}Fe Mössbauer spectra for **5** (e) and **5**@$NH_{3(g)}$ (f).[53]

gradual transitions upon cooling. Furthermore, dynamic subcomponent exchange was demonstrated: electron-rich amines could efficiently displace electron-deficient ones, enabling post-synthetic cage-to-cage transformation without loss of stereochemical integrity. This work demonstrates the versatility of chiral subcomponent assembly in producing structurally well-defined, enantiopure SCO cages with tunable magnetic properties and dynamic structural responsiveness.

In 2016, Gu and co-workers presented the first example of single-crystal-to-single-crystal (SCSC) metal-center exchange in a $Fe(II)_4L_6$ cage, offering a novel post-synthetic strategy for tuning SCO behavior in discrete polynuclear systems.[80] A porous $Ni(II)_4L_6$ cage featuring one-dimensional supramolecular channels was synthesized, enabling Fe(II) ions to diffuse into the crystal lattice and gradually replace Ni(II) centers to afford Fe/Ni-mixed cages (FeNi-1 to FeNi-3) while retaining crystallinity and cage integrity (Fig. 9a–e). In contrast, the non-porous $Fe(II)_4L_6$ cage (**9**) with densely packed structure did not permit metal exchange. Magnetic susceptibility data at 298 K revealed an increase in χ_mT from

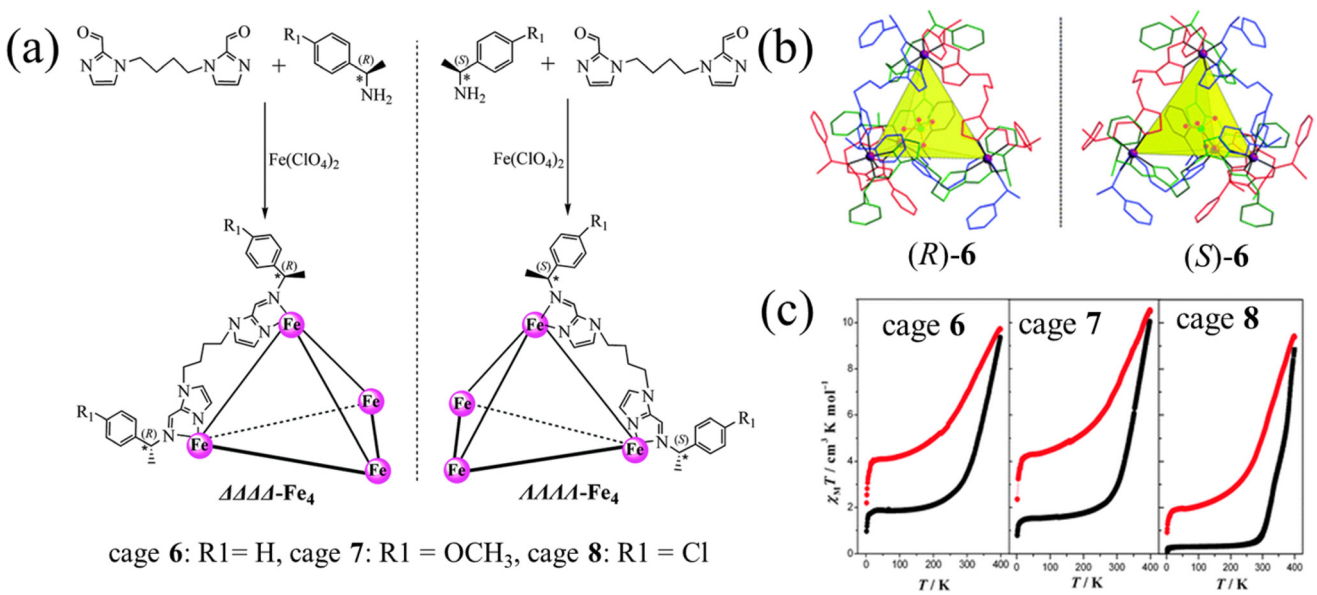

Fig. 8 (a) Synthesis method of **6**–**8**. (b) Crystal structures of **6**. (c) χ_mT *vs.* *T* plots for **6**–**8**.[79]

5.60 cm^3 K mol^{-1} (FeNi-1) to 6.78 cm^3 K mol^{-1} (FeNi-2) and 7.37 cm^3 K mol^{-1} (FeNi-3), reflecting progressive incorporation of Fe(II) centers. Notably, only FeNi-3 (Fe : Ni ≈ 1 : 1) showed partial SCO behavior, with its $\chi_m T$ value decreasing from 8.06 cm^3 K mol^{-1} at 400 K to 7.37 cm^3 K mol^{-1} at 290 K and remaining nearly constant thereafter, indicating that only ~11.5% of the Fe(II) centers undergo thermal spin transition (Fig. 9f). Mössbauer spectroscopy of FeNi-3 at 80 K further confirmed the coexistence of HS (δ = 1.17 mm·s^{-1}, ΔE_Q = 2.86 mm s^{-1}) and LS (δ = 0.37 mm s^{-1}, ΔE_Q = 0.49 mm s^{-1}) Fe(II) species, with a HS population of approximately 86.8%. This work demonstrates that SCSC metal exchange, governed by crystal porosity and diffusion pathways, offers a rare and effective approach to modulate SCO profiles in cage-based materials without compromising structural integrity.

In 2019, Li and co-workers reported a mixed-spin SCO $Fe(II)_4L_6$ cage (**10**), assembled from a bis-bidentate thiazolylimine ligand and $Fe(BF_4)_2{\cdot}6H_2O$ in acetonitrile (Fig. 10a).[81] SXRD revealed that each cage adopts *T*-symmetric tetrahedral geometry, with six bis-bidentate ligands bridging four Fe(II) centers (Fig. 10b). The cage encapsulates a central BF_4^- anion within its cavity and exists as enantiomeric pairs (ΔΔΔΔ and ΛΛΛΛ configurations). Structural analysis at 100 K confirmed a [LS–LS–LS–HS] configuration, as confirmed by Fe–N bond length and distortion parameters. Variable-temperature SQUID magnetometry demonstrated a gradual and reversible SCO behaviour with significant thermal hysteresis (Fig. 10c). Upon cooling from 400 K to 100 K, the $\chi_m T$ value declined from 9.95 to ~3.0 cm^3 K mol^{-1}, corresponding to an incomplete transition to the LS state. The transition temperatures were $T_{1/2\downarrow}$ = 311 K and $T_{1/2}{}^{\uparrow}$ = 340 K, giving a thermal hysteresis width of 29 K. This behavior indicates a spin-state distribution change from [3HS–1LS] to [3LS–1HS] upon cooling. Furthermore, variable-temperature X-ray photoelectron spectroscopy (VT-XPS) on a thin film of cage **10** allowed quantification of spin states at the surface. Calibrated against SQUID data, the VT-XPS revealed that only ~35% of Fe(II) centers on the surface undergo SCO, compared to 58% in the bulk (Fig. 10d). This difference is attributed to surface effects such as lattice relaxation and reduced cooperativity. The study represents the first application of VT-XPS to SCO cages and reveals distinct magnetic behaviors between surface and bulk states. In addition, this work is significant for future implementation of SCO cages in spintronic devices and surface-confined molecular materials.

In 2019, Gu and co-workers prepared a rare supramolecular zeolite framework with LTA topology constructed from a tetrahedral cage (**11**) and ClO_4^- anions.[82] The cage was self-assembled from a tris(imidazole-imine) ligand and $Fe(ClO_4)_2$ in acetonitrile, yielding air-stable dark purple crystals (Fig. 11a). SXRD at 173 K revealed that each cage contains four Fe(II) centers coordinated by six C_2-symmetric bis-bidentate ligands, with an Fe–Fe distance of 9.59 Å (Fig. 11b). The average Fe–N bond length of 1.98 Å is consistent with a LS Fe(II) configuration. Notably, these cages further assembled *via* electrostatic interactions with ClO_4^- anions to generate a 3D zeolite-like framework, comprising double 4-rings, truncated octahedra (β-cages), and cuboctahedra (α-cages), thereby mimicking the classic LTA zeolite structure (Fig. 11c–j). Magnetic measurements revealed a gradual and incomplete SCO transition between 2 and 400 K (Fig. 11k). The $\chi_m T$ value increased from low values at 2 K to 11.20 cm^3 K mol^{-1} at 400 K, with a transition

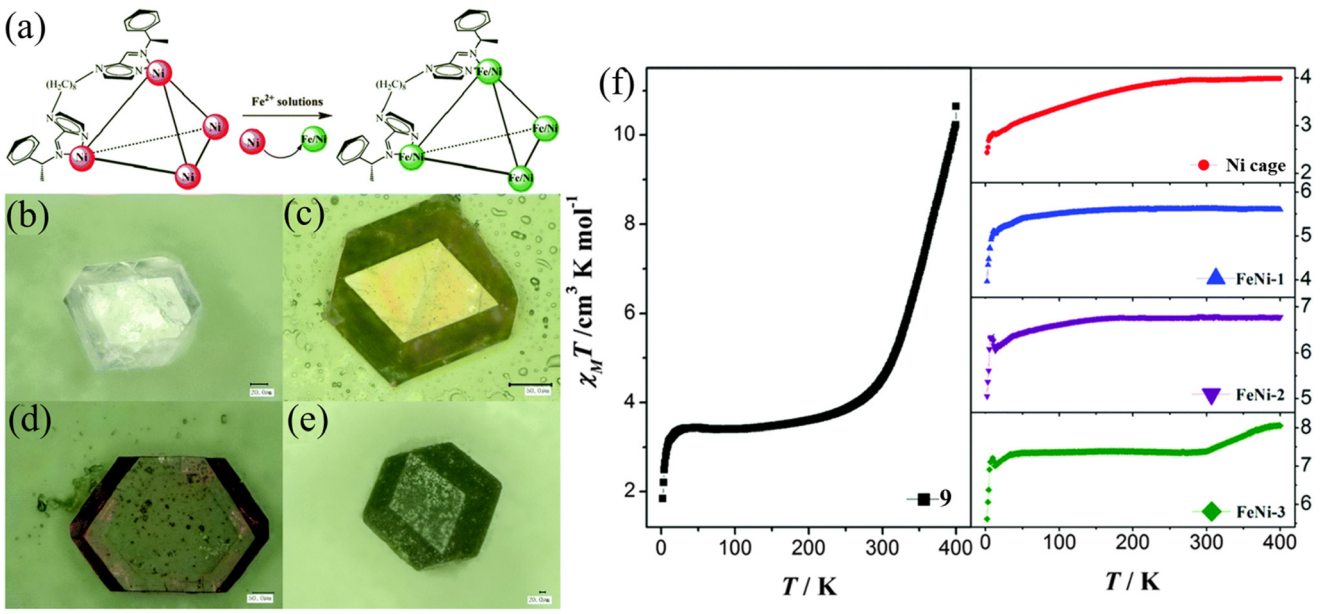

Fig. 9 (a) Synthesis method of FeNi cages. Optical microscopic photos of (b) Ni cage, (c) FeNi-1, (d) FeNi-2, (e) FeNi-3. (f) $\chi_m T$ *vs.* *T* plots for different cage complexes.[80]

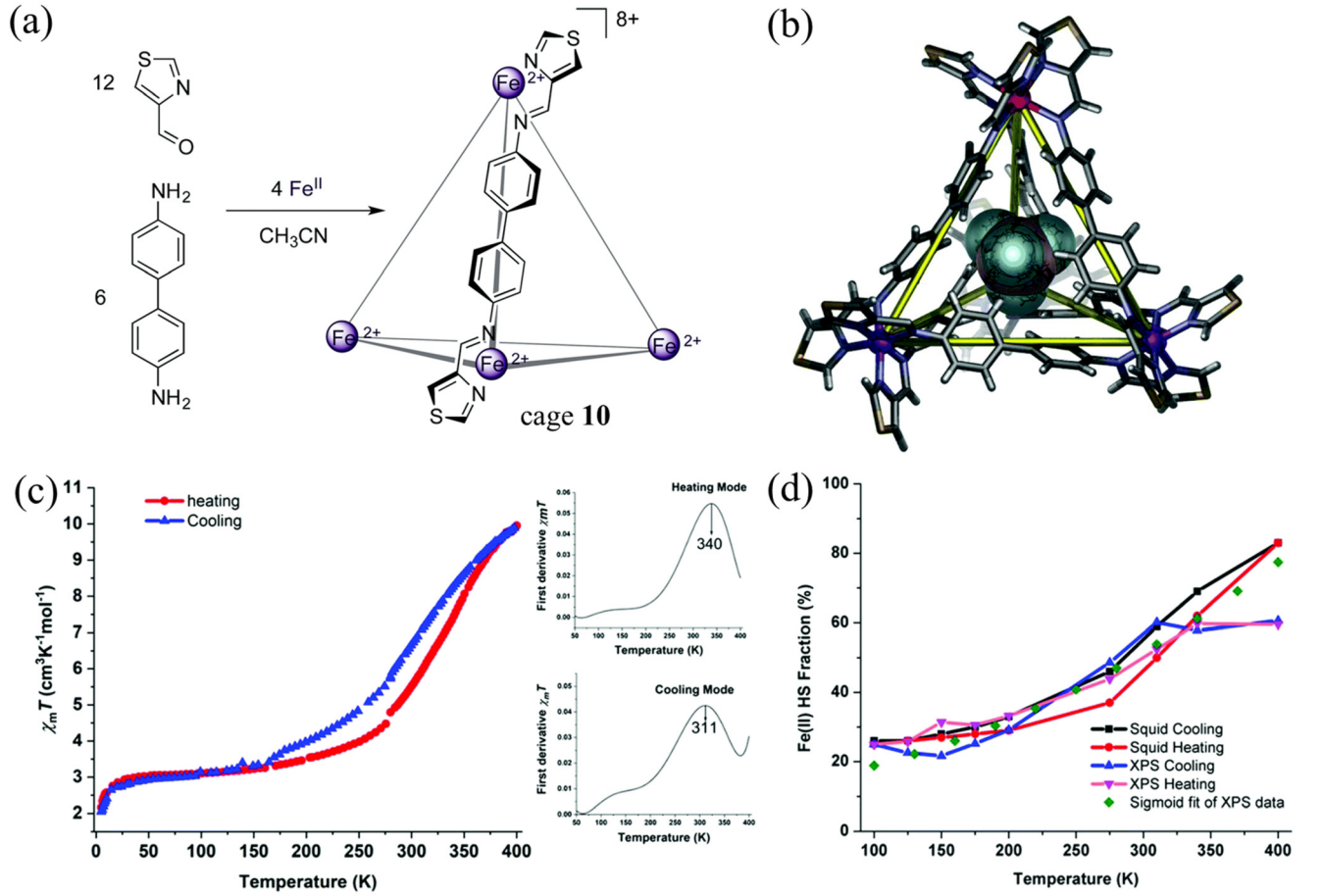

Fig. 10 Synthesis method (a) and crystal structure (b) of cage **10**. $\chi_m T$ *vs.* *T* plots for cage **10** (c). The inserts are the first derivative of magnetic susceptibility curves. (d) Overlay of XPS data (calibrated based on SQUID data) with the corresponding fitted sigmoid curve.[81]

temperature estimated at 321 K. This corresponds to the switching of Fe(II) centers from the LS to HS state. Upon guest inclusion (iodine vapor or anionic dyes such as Amaranth and Congo Red), the SCO behavior of **11** was completely suppressed. The disruption of SCO is attributed to multiple host–guest interactions, including charge-transfer, π–π stacking, and hydrogen bonding between the cage framework and the guest molecules. This study demonstrates the feasibility of assembling zeolite-type frameworks from discrete SCO cages and highlights the role of guest encapsulation in regulating their magnetic bistability.

In 2018, Gu *et al.* reported two Fe(II)$_4$L$_6$ cages (cages **12** and **13**) featuring rare cube-like cavities, designed for selective inclusion of fullerene molecules and exhibiting guest-responsive SCO properties.[83] The cages were assembled from flexible di(imidazole aldehyde) ligands containing *O*-benzene (cage **12**) or *O*-naphthalene (cage **13**) units, combined with (*R*)-1-(naphthalen-2-yl)ethanamine and $Fe(OTf)_2$ in acetonitrile (Fig. 12a). SXRD revealed edge-bridged tetrahedral architectures with *T* point group symmetry. The average Fe–N bond lengths are 1.96 Å (cage **12**) and 1.98 Å (cage **13**), suggesting a LS electronic configuration of Fe(II) at 173 K (Fig. 12b). The flexible linkers enabled rotation and distortion, producing unusual cube-like cavities enclosed by π-rich aromatic walls, suitable for C_{60} binding *via* π–π and donor–acceptor interactions. Encapsulation of C_{60} was confirmed by NMR and HRMS, with formation of [C_{60}@**12**] and [C_{60}@**13**] host–guest complexes. Cage **12** exhibited stronger affinity for C_{60} due to better shape complementarity, whereas neither cage showed appreciable binding to C_{70}, consistent with Rebek's 55% volume rule. Solid-state magnetic susceptibility measurements revealed that both cages displayed incomplete and gradual SCO behavior, with $T_{1/2}$ = 344 K for **12** and 328 K for **13** (Fig. 12c and d). Upon C_{60} inclusion, $T_{1/2}$ decreased to 312 K and 306 K, respectively, indicating stabilization of the HS state (Fig. 12c and d). Furthermore, abnormal increases in $\chi_m T$ values at low temperatures (*e.g.*, up to 4.16 cm^3 K mol^{-1} at ~50 K) were observed in the C_{60}-bound complexes, likely arising from exchange interactions between C_{60} π-electrons and Fe(II) centers, suggesting the emergence of guest-mediated magnetic communication. This study demonstrates that the interplay between structural flexibility and guest binding can effectively modulate the SCO behavior of Fe(II)$_4$L$_6$ cages, establishing a versatile platform for magnetic host–

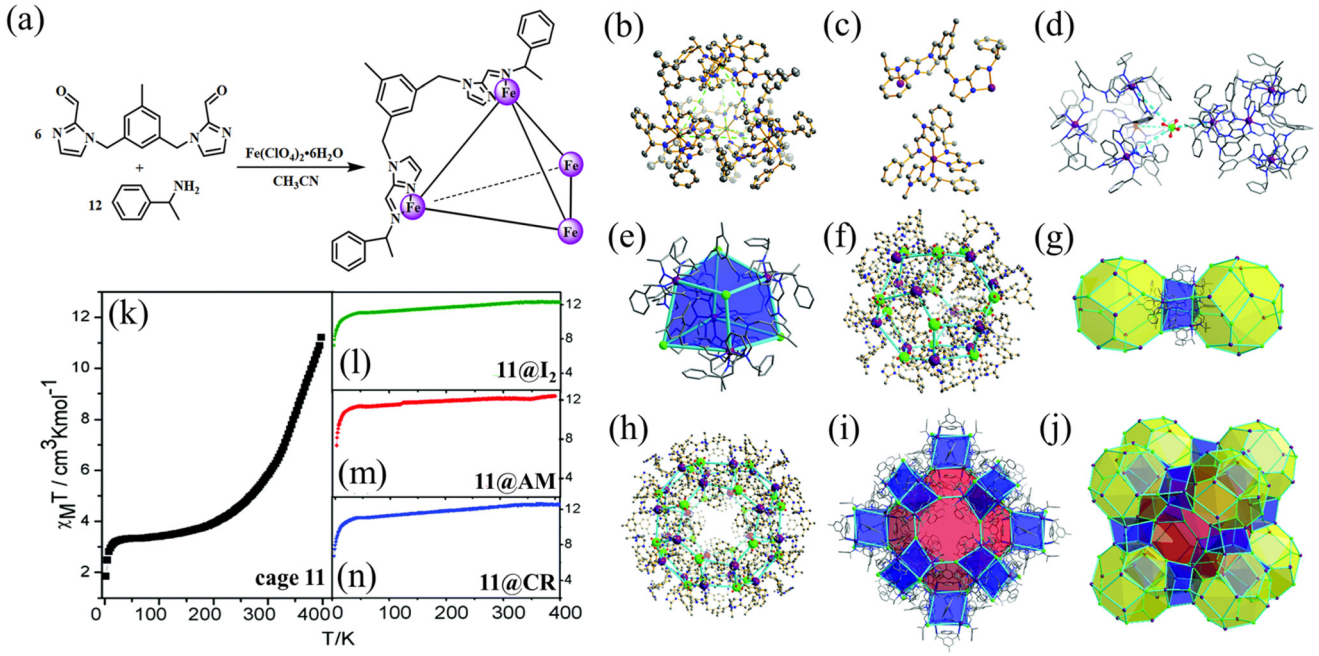

Fig. 11 Synthesis method (a) and crystal structure of cage **11** (b). (c) One edge and one vertex of cage **11**. (d) Two adjacent cages bridged through a ClO_4^- anion. (e) Diagram of double 4-rings. (f) Diagram of β-cage. (g) Diagram of two β-cage attached to a double 4-rings. (h) Diagram of α-cage. (i) Diagram of 12 double-4 rings around each α-cage. (j) Diagram of LTA topology. $\chi_m T$ *vs.* *T* plots for **11** (k), **11**@I_2 (l), **11**@AM (m) and **11**@CR (n).[82]

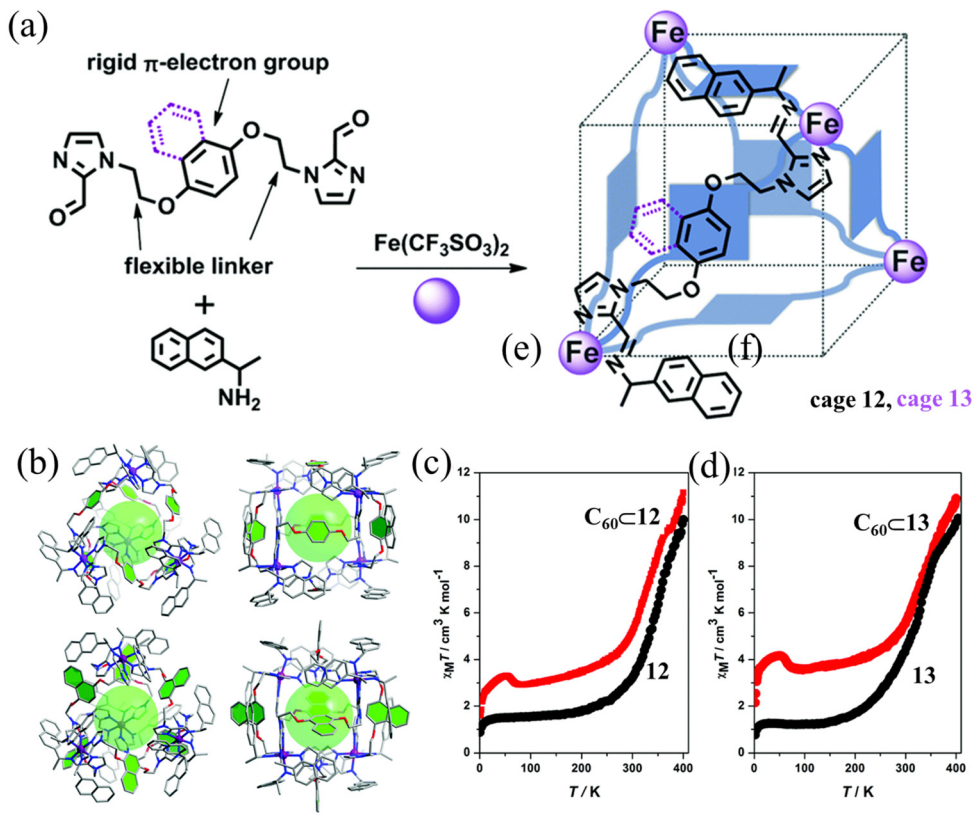

Fig. 12 (a) Synthesis method of cages **12** and **13**. (b) Crystal structures of **12** (top) and **13** (bottom). $\chi_m T$ *vs.* *T* plots for **12** and C_{60}⊂**12** (c) and **13** and C_{60}⊂**13** (d).[83]

guest systems with potential in fullerene recognition and sensing technologies.

In 2020, Tanaka *et al.* reported two structurally well-defined tetrahedral $Fe(II)_4L_6$ cages, termed as **14** and **15**.[84] SXRD revealed symmetric tetrahedral architectures in which four Fe(II) centers occupy the vertices and are bridged by six bis-bidentate ligands (Fig. 13a–c and e). The internal cavities are densely filled with phenylene spacers, leaving no accessible space for guest inclusion. Each Fe center is coordinated facially by three chelating imidazole-imine donors, with average Fe–N distances of 2.11–2.25 Å at 113 K, characteristic of HS Fe(II). In contrast to many previously reported SCO cages,[89,90] these structures are achiral, possessing S_4 symmetry with two Δ and two Λ configurations. Magnetic susceptibility measurements (5–300 K) on desolvated samples demonstrated gradual but incomplete SCO in both complexes (Fig. 13d). The incomplete SCO is attributed to the rigid, π-stacked phenylene framework that imposes steric constraints preventing full Fe–N bond contraction during spin transition. Notably, cage **15** shows a slightly higher transition temperature than cage **14**, consistent with the stronger ligand field imparted by electron-donating methyl substituents. Electrochemical studies showed quasi-reversible Fe(II)/Fe(III) redox couples at 0.61 V for **14** and 0.48 V for **15** (*vs.* Fc^+/Fc), further supporting the stronger donor ability of methylated ligands (Fig. 13f and g). These findings highlight how subtle variations in ligand electronics can significantly affect SCO behavior in Fe(II) cages, offering useful design principles for future development of responsive host-guest and magneto-electrochemical systems.

In 2022, Garcia and co-workers reported the first $Fe(II)_4L_6$ SCO cage based on pyridyl–hydrazone ligand scaffolds, synthesized *via* subcomponent self-assembly of $Fe(BF_4)_2{\cdot}6H_2O$, *N*,*N*-diaminonaphthalenetetracarboxydiimide, and 2-formylpyridine in a 4 : 6 : 12 stoichiometry[85] (**16**) (Fig. 14a). SXRD at 120 K revealed a symmetric tetrahedral architecture with each Fe(II) center octahedrally coordinated by three bis-bidentate ligands, forming FeN_6 environments (Fig. 14b). The Fe–N bond lengths (1.98–2.00 Å) confirm a LS configuration at low temperature. The solid-state structure was stabilized by peripheral hydrogen bonds and extensive π–π interactions between adjacent cages. Magnetic susceptibility measurements (2–400 K) on desolvated crystals revealed a gradual and incomplete SCO behavior (Fig. 14c). Upon cooling from 400 K to 100 K, the $\chi_m T$ value declined from 12.49 to 5.44 cm^3 $K\ mol^{-1}$, with no thermal hysteresis. Mössbauer spectroscopy at 80 K showed two quadrupole doublets: a dominant LS Fe(II) species (δ = 0.45 mm s^{-1}, ΔE_Q = 0.36 mm s^{-1}, A = 62%) and a HS component (δ = 1.17 mm s^{-1}, ΔE_Q = 3.12 mm s^{-1}, A = 38%), confirming partial SCO (Fig. 14d). DFT calculations revealed that the incorporation of electron-withdrawing carbonyl groups near the coordination site lowers the energy gap between HS and LS states, rationalizing the observed SCO in contrast to analogous pyridyl–imine cages, which remain LS. Thermodynamically, the Gibbs free energy difference ΔG_{HS-LS} shifts from favoring the LS state at 2 K to slightly favoring the HS state at 400 K, consistent with experimental findings. This work introduces a new ligand platform for SCO cage design and demonstrates that fine-tuning coordination environments *via* functional group modification can promote SCO in systems previously considered magnetically silent.

Building on this, the Garcia group investigated the gas sensing behavior of cage **16** using microcrystalline samples.[91] Magnetic susceptibility measurements show that the SCO behavior of **16** in the microcrystalline state is similar to that in the crystalline state (Fig. 15a). Upon exposure to $NH_{3(g)}$, the microcrystalline cage exhibited a rapid and visible color change from light purple to dark gray within 90 s (Fig. 15b). ^{57}Fe Mössbauer spectroscopy confirmed a complete conversion to the LS state: in the pristine sample, three distinct quadrupole doublets were observed, corresponding to two HS species (δ = 0.95 mm s^{-1}, ΔE_Q = 2.00 mm s^{-1}; δ = 1.07 mm s^{-1}, ΔE_Q = 2.74 mm s^{-1}) and one LS species (δ = 0.37

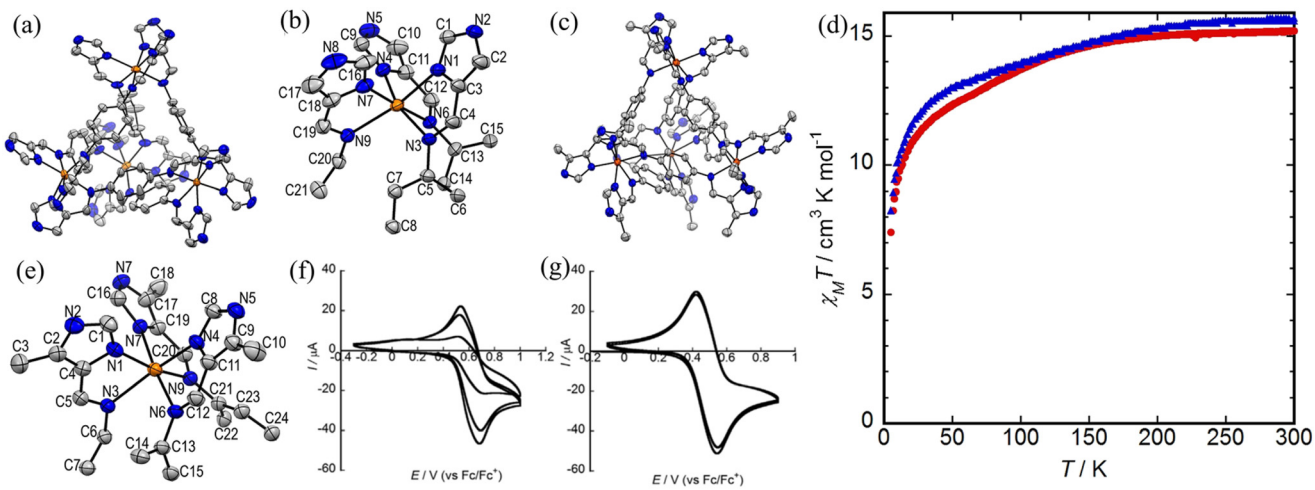

Fig. 13 Crystal structures of **14** (a) and **15** (c) and their corresponding asymmetric units (b and e). (d) $\chi_m T$ *vs.* T plots for **14** (red) and **15** (blue). Cyclic voltammograms of **14** (f) and **15** (g). Adapted from ref. 84.

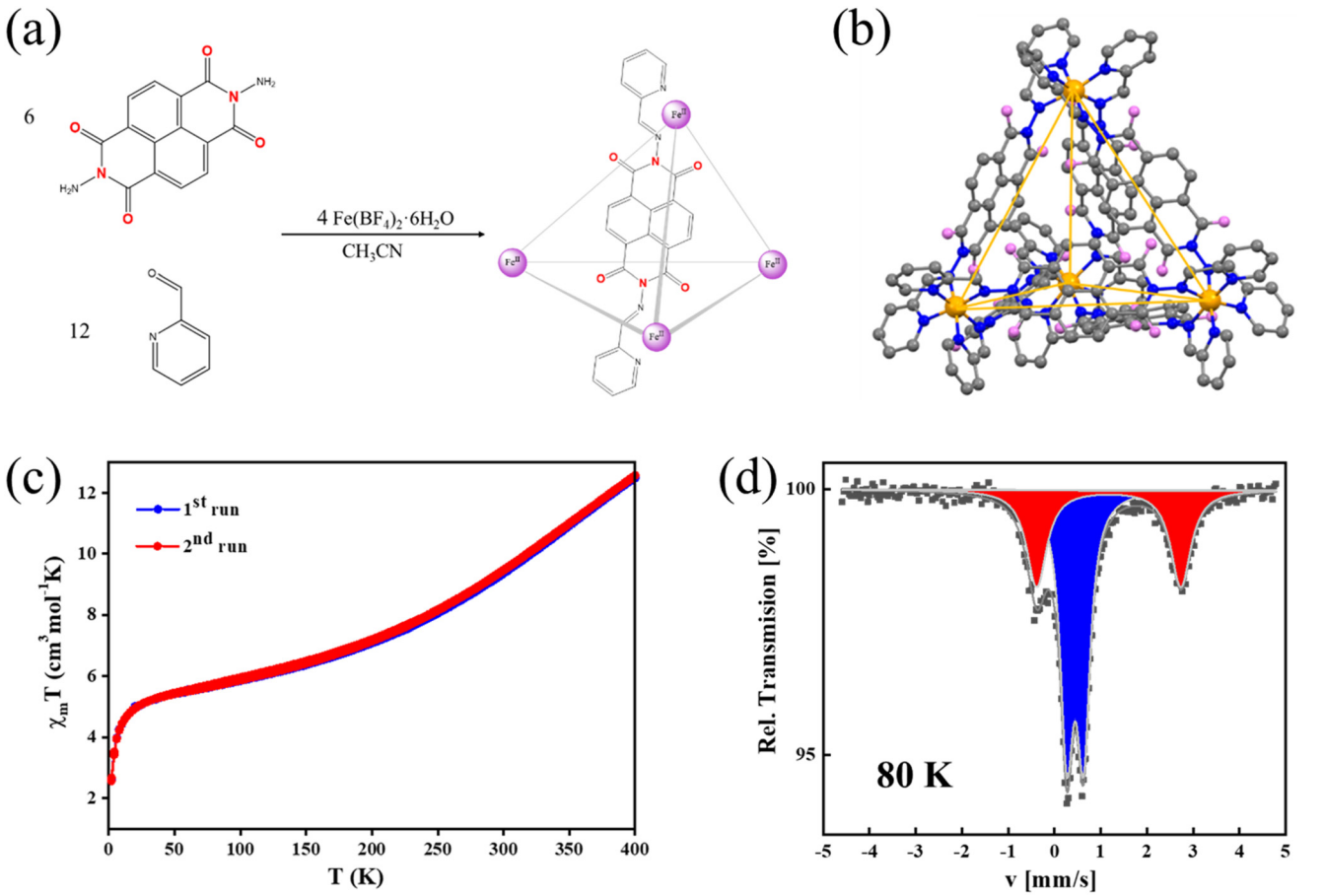

Fig. 14 Synthesis method (a) and crystal structure (b) of **16**. (c) $\chi_m T$ *vs.* *T* plots for **16**. (d) ^{57}Fe Mössbauer spectrum of **16**.[85]

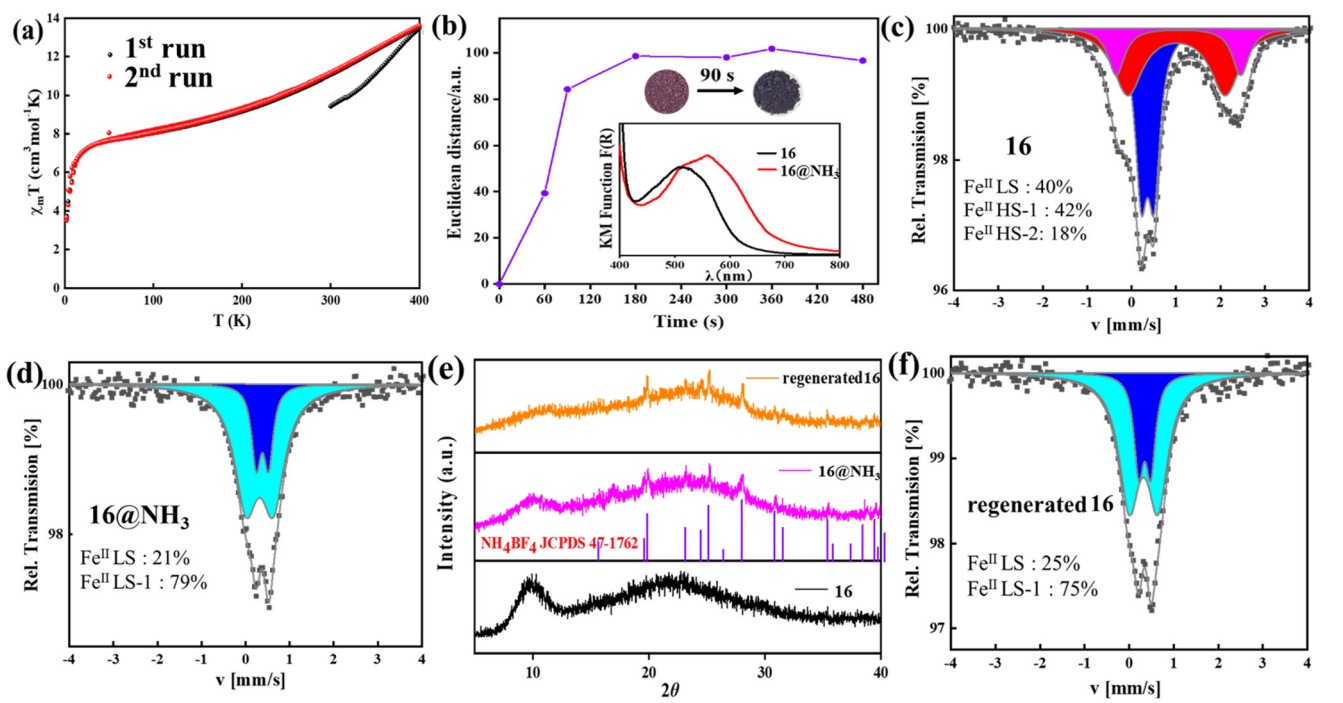

Fig. 15 (a) $\chi_m T$ *vs.* *T* plots for microcrystalline cage **16**. (b) Response time curve of **16** to $NH_{3(g)}$ at room temperature. ^{57}Fe Mössbauer spectrum of **16** (c), **16**@NH_3 (d) and regenerated **16** (f). PXRD patterns of **16**, **16**@NH_3 and regenerated **16** (e).[91]

mm s^{-1}, ΔE_Q = 0.30 mm s^{-1}), in a 41% : 59% HS : LS ratio (Fig. 15c). After $NH_{3(g)}$ exposure, only LS signals remained, including a new LS species (δ = 0.32 mm s^{-1}, ΔE_Q = 0.62 mm s^{-1}), attributed to direct coordination of NH_3 to Fe(II) centers (Fig. 15d). The sensing process was accompanied by *in situ* formation of NH_4BF_4 through reaction between $NH_{3(g)}$, water, and lattice BF_4^- anions (Fig. 15e). Notably, the Mössbauer spectrum of regenerated **16** collected after dynamic vacuum/heating shows the same all-LS pattern, confirming that the NH_3-induced transition is effectively irreversible (Fig. 15f).

In 2024, Garcia *et al.* further developed two new $Fe(II)_4L_6$ cages (**17**–**18**) based on cage **16** constructed *via* subcomponent self-assembly using a pyridyl–hydrazone coordination mode and different anions (ClO_4^- and $CF_3SO_3^-$) to systematically investigate solvent and anion effects on SCO behavior (Fig. 16a).[86] SXRD confirmed that all cages adopt edge-bridged tetrahedral architectures and octahedral FeN_6 coordination environments (Fig. 16b and c). The observed Fe–N bond distances (1.96–2.00 Å) and $\sum$ parameters (~62.8°) are consistent with a LS Fe(II) state at low temperature (Fig. 16b and c). Magnetic susceptibility measurements revealed gradual and incomplete SCO for all three cages, with desolvated samples showing higher $\chi_m T$ values than solvated analogues, indicating that solvent molecules stabilize the LS state (Fig. 16d). For **18**·desolvated, the $\chi_m T$ value reaches 12.40 cm^3 K mol^{-1} at 400 K and decreases to 6.03 cm^3 K mol^{-1} at 50 K, indicating a [2HS–2LS] spin-state distribution (Fig. 16e). Cage **17** (ClO_4^-) exhibited

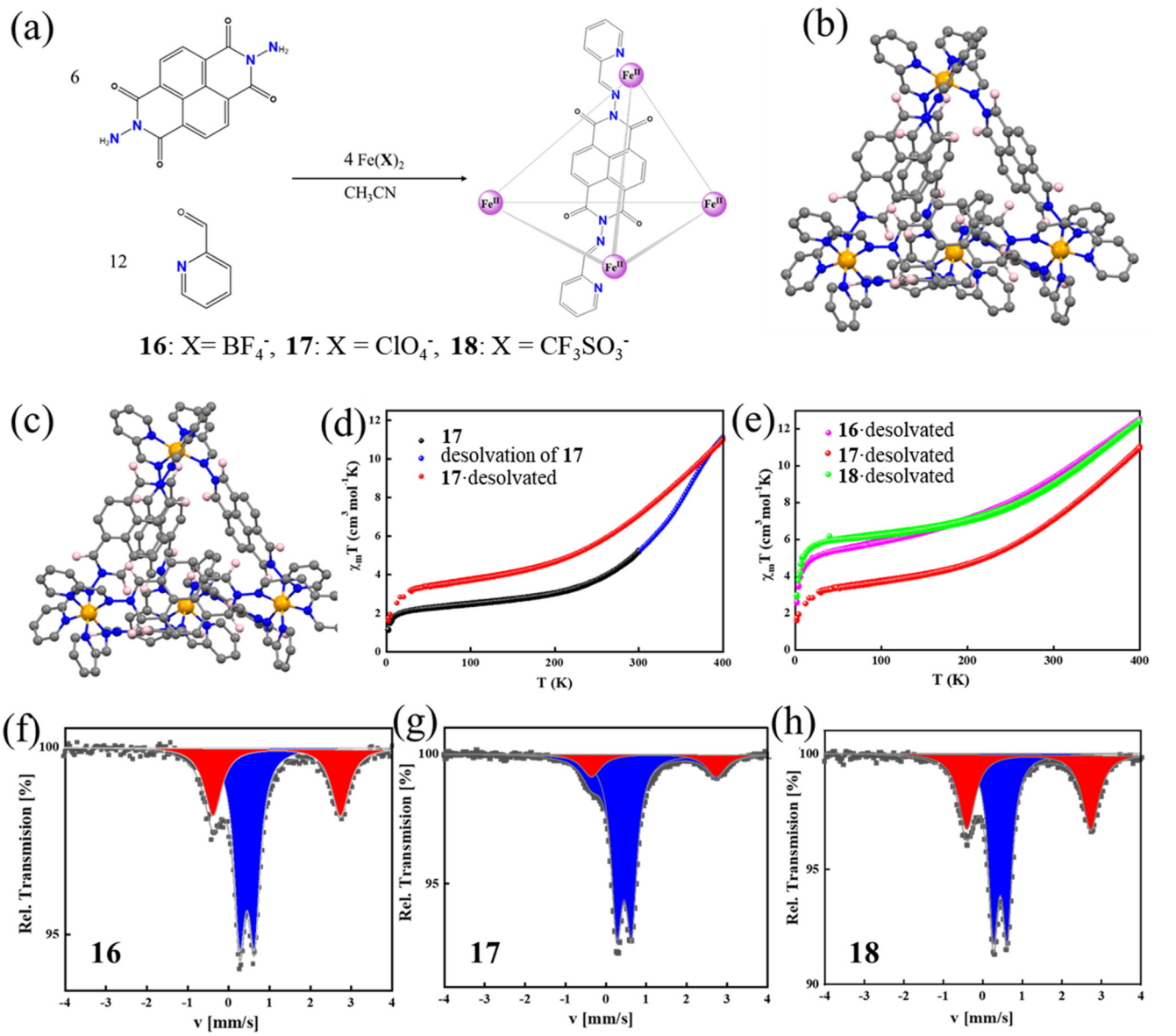

Fig. 16 (a) Synthesis method of cages **16**–**18**. Crystal structures of **17** (b) and **18** (c). (d) $\chi_m T$ *vs.* *T* plots for **17** (black circles), desolvation of **17** (blue circles) and **17**·desolvated (red circles). (e) $\chi_m T$ *vs.* *T* plots for desolvated **16**–**18**. ^{57}Fe Mössbauer spectra of desolvated **16** (f), **17** (g) and **18** (h) recorded at 80 K.[86]

the lowest $\chi_m T$ (3.42 cm^3 K mol^{-1} at 50 K) and was assigned a [1HS–3LS] configuration (Fig. 16e). Mössbauer spectra at 80 K confirmed these observations: for **16–18**, the relative areas of LS/HS species were 62% : 38%, 80% : 20%, and 56% : 44%, respectively, with typical parameters (LS: δ = 0.45 mm s^{-1}, ΔE_Q = 0.36 mm s^{-1}; HS: δ = 1.17 mm s^{-1}, ΔE_Q = 3.12 mm s^{-1}) (Fig. 16f–h). To rationalize these results, DFT calculations were performed on spin isomers of the $[Fe_4L_6]^{8+}$ core and simplified mono-Fe models including anions. The calculated energy gaps between HS and LS states reproduced the experimentally observed trends, with cage **17** exhibiting the largest LS stabilization (ΔG_{HS-LS} = −0.9 kcal mol^{-1}). Theoretical Mössbauer parameters matched well with experimental data, supporting model validity. Analysis showed that although the anions do not significantly perturb the FeN_6 core geometry or Fe d-orbitals, ClO_4^- anions display slightly stronger interactions with LS states, rationalizing the observed spin-state distribution differences. These studies underscore the critical role of counter anions and solvents in modulating SCO behavior in Fe(II) cages.

In 2025, Gupta and co-workers synthesized three $Fe(II)_4L_6$ tetrahedral cages (**19–21**) *via* subcomponent self-assembly, using 4,4′-diaminobiphenyl, pyridine-2-carboxaldehyde, and FeX_2 salts (X = BF_4^-, ClO_4^-, NTf_2^-) (Fig. 17a).[87] This work demonstrates that variations in anion identity and ligand conformation directly influence the diastereomeric distribution (T, S_4, and C_3) (Fig. 17b–d) in both solid and solution phases, which in turn has a significant impact on the SCO behavior of the resulting cages. Solid-state magnetic susceptibility measurements revealed that **19** and **20**, dominated by the homochiral *T*-isomer, show nearly identical, gradual and incomplete SCO behaviors, with $\chi_m T$ values increasing from ~3.8 cm^3 K mol^{-1} at 3 K to ~7.8 cm^3 K mol^{-1} at 380 K, corresponding to ~54% HS population (Fig. 17e and f). In contrast, **21**, enriched in the S_4-isomer and associated with bulkier NTf_2^- anions, displayed a delayed and weaker spin transition with $\chi_m T$ rising only from 2.74 to 4.72 cm^3 K mol^{-1} over the same temperature range (Fig. 17g). In solution, variable-temperature ^{1}H NMR (Evans method) and UV-vis spectroscopy further confirmed that the spin transition temperatures follow the trend $T_{1/2}$ (**19**) < $T_{1/2}$ (**20**) < $T_{1/2}$ (**21**), consistent with increasing LS stabilization due to decreased steric bulk around the Fe(II) centers in S_4 and C_3 dominated cages. This work underscores the critical role of diastereomeric distribution and ligand geometry in determining the magnetic behavior of SCO-active cages, and provides valuable design insights into the use of structural isomerism as a strategy to tune spin-state equilibria.

4. Conclusions and perspectives

In conclusion, tetrahedral Fe(II)-based metal organic cages have gained increasing attention as versatile SCO systems, owing to their unique ability to combine magnetic bistability with host–guest chemistry. Recent advances in ligand design and self-assembly strategies have enabled the construction of both face-capped $Fe(II)_4L_4$ and edge-bridged $Fe(II)_4L_6$ architectures, which display diverse SCO behaviors under thermal, chemical, or photonic stimuli. These cages serve as valuable models for understanding how factors such as ligand field strength, intermolecular interactions and guest encapsulation influence spin-state switching and distribution. Through a combination of magnetic susceptibility, Mössbauer spectroscopy, and crystallographic analysis,

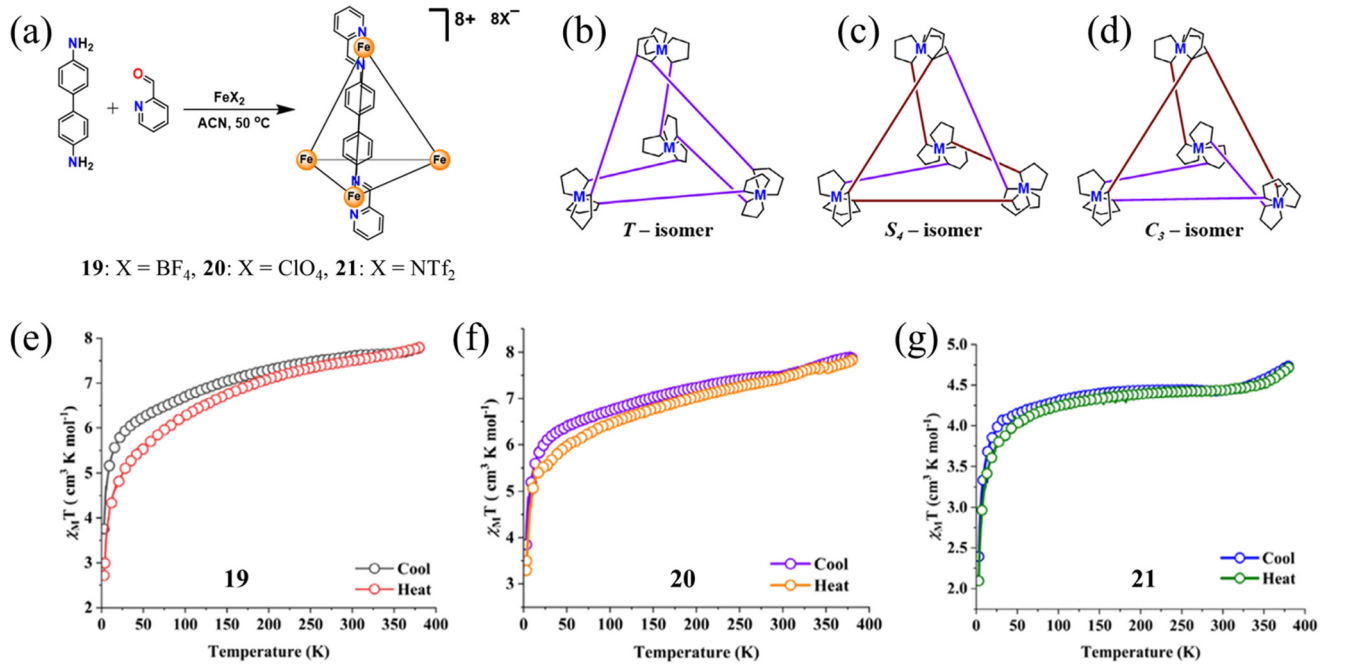

Fig. 17 (a) Synthesis method of cages **19–21**. (b–d) Diagrams of three diastereomers. $\chi_m T$ *vs.* *T* plots for **19** (e), **20** (f) and **21** (g). Adapted from ref. 87.

structure–function relationships have been systematically established. In addition, we also summarized emerging solid-state applications of these SCO cages, such as gas sensing and guest-responsive adsorption. These studies demonstrate the potential of Fe(II) SCO cages not only for probing fundamental structure–property relationships, but also for developing functional materials that integrate magnetic, optical, and host-guest responsiveness in the solid state.

Despite these advances, several key challenges remain. (i) Achieving cooperative and abrupt SCO transitions with thermal hysteresis in cage systems remains rare due to the limited intermolecular coupling in discrete structures. (ii) Rational prediction of SCO behavior based on ligand design is still not an easy task, as small structural changes can lead to dramatic and sometimes unpredictable magnetic responses. (iii) Maintaining crystallinity and structural integrity remains a major challenge, as these supramolecular cages often contain a large amount of lattice solvent. The loss or exchange of solvent, especially during SXRD measurements, can easily lead to crystal cracking, structural collapse, or loss of long-range order. This prevents accurate structural characterization and complicates the correlation between molecular structure and SCO behavior.

In the future, the research on SCO-active Fe(II) cages is expected to achieve further development through a wider range of design strategies and functional integration. (i) Diversifying ligand structures beyond specific motifs such as imidazole-, pyridyl-, or hydrazone-based donors will be essential for enriching cage geometries, tuning ligand field strength, and enabling new SCO profiles. Ligand electronic effects, conformational flexibility, and steric bulk all provide useful handles to modulate spin-state energetics and cooperativity. (ii) Controlling cage structural parameters such as Fe–Fe distance and internal cavity volume by varying ligand length, structure and connectivity provides a way to tune SCO behavior and guest binding properties. This opens up new possibilities for dual-responsive systems that combine magnetic bistability with molecular recognition or encapsulation. (iii) Transforming molecular cages into functional materials such as thin films, composites, or sensor arrays represents a promising path to practical applications. Combining SCO cages with optical readout methods or electronic interfaces is expected to construct real-time and reversible small molecule sensing platforms, especially in the solid state.

Author contributions

Y. G. supervised and designed the project. W. L. and X. L. conducted literature research and wrote the manuscript. M. W. and Y. B. offered guidance on data visualization.

Conflicts of interest

The authors declare that they have no competing interest in this work.

Data availability

Data are available upon reasonable request.

Acknowledgements

This work was supported through the Fonds De La Recherche Scientifique—FNRS (PDR T.0095.21, CDR J.0064.23, EQP U. N027.24) and the Talent Scientific Research Fund of Liaoning Petrochemical University (No. 2024XJJL-026). W. L. and X. L. were supported by fellowships from the China Scholarship Council (201908310083, 202108310050).

References

1 Y. Zhang, R. Torres-Cavanillas, X. Yan, Y. Zeng, M. Jiang, M. Clemente-León, E. Coronado and S. Shi, *Chem. Soc. Rev.*, 2024, **53**, 8764–8789.
2 S. Xue, Y. Guo and Y. Garcia, *CrystEngComm*, 2021, **23**, 7899–7915.
3 R. Torres-Cavanillas, M. Gavara-Edo and E. Coronado, *Adv. Mater.*, 2024, **36**, 2307718.
4 S. Z. Zhao, H. W. Zhou, C. Y. Qin, H. Z. Zhang, Y. H. Li, M. Yamashita and S. Wang, *Chem. – Eur. J.*, 2023, **29**, e202300554.
5 J. Villalva, A. Develioglu, N. Montenegro-Pohlhammer, R. Sánchez-de-Armas, A. Gamonal, E. Rial, M. García-Hernández, L. Ruiz-Gonzalez, J. S. Costa and C. J. Calzado, *Nat. Commun.*, 2021, **12**, 1578.
6 A. Bousseksou, G. Molnár, L. Salmon and W. Nicolazzi, *Chem. Soc. Rev.*, 2011, **40**, 3313–3335.
7 J. Linares, E. Codjovi and Y. Garcia, *Sensors*, 2012, **12**, 4479–44928.
8 G. Molnár, S. Rat, L. Salmon, W. Nicolazzi and A. Bousseksou, *Adv. Mater.*, 2018, **30**, 1703862.
9 S. Kamilya, B. Dey, K. Kaushik, S. Shukla, S. Mehta and A. Mondal, *Chem. Mater.*, 2024, **36**, 4889–4915.
10 K. Ridier, A. Hoblos, S. Calvez, M. Lorenc, W. Nicolazzi, S. Cobo, L. Salmon, L. Routaboul, G. Molnár and A. Bousseksou, *Coord. Chem. Rev.*, 2025, **535**, 216628.
11 P. Gütlich, A. B. Gaspar and Y. Garcia, *Beilstein J. Org. Chem.*, 2013, **9**, 342–391.
12 B. Dey and V. Chandrasekhar, *Dalton Trans.*, 2022, **51**, 13995–14021.
13 J. Olguín, *Coord. Chem. Rev.*, 2020, **407**, 213148.
14 L. Zhao, Y.-S. Meng, Q. Liu, O. Sato, Q. Shi, H. Oshio and T. Liu, *Nat. Chem.*, 2021, **13**, 698–704.
15 G. Yang, Z. Y. Ruan, Y. C. Chen, P. Y. Liao, S. G. Wu, Z. P. Ni and M. L. Tong, *Angew. Chem., Int. Ed.*, 2025, e202414330.
16 Y.-R. Chen, T.-T. Ying, Y.-C. Chen, P.-Y. Liao, Z.-P. Ni and M.-L. Tong, *Chem. Sci.*, 2024, **15**, 9240–9248.
17 K. Madeja and E. König, *J. Inorg. Nucl. Chem.*, 1963, **25**, 377–385.
18 G. Yang, Z.-P. Ni and M.-L. Tong, *Coord. Chem. Rev.*, 2024, **521**, 216146.
19 O. A. Qamar, F. Jamil, M. Hussain, M. Mustafa, R. U. Rehman, A. Inayat, M. S. Habib and M. Sajid, *Chem. Pap.*, 2023, **77**, 7331–7359.

20 M. K. Javed, A. Sulaiman, M. Yamashita and Z.-Y. Li, *Coord. Chem. Rev.*, 2022, **467**, 214625.
21 K. Sun, J.-P. Xue, Z.-S. Yao and J. Tao, *Dalton Trans.*, 2022, **51**, 16044–16054.
22 V. Kumar, A. Rotaru and Y. Garcia, *J. Mater. Chem. C*, 2022, **10**, 14128–14134.
23 E. Resines-Urien, E. Fernandez-Bartolome, A. Martinez-Martinez, A. Gamonal, L. Piñeiro-López and J. S. Costa, *Chem. Soc. Rev.*, 2023, **52**, 705–727.
24 O. Kahn and C. J. Martinez, *Science*, 1998, **279**, 44–48.
25 T. Gebretsadik, Q. Yang, J. Wu and J. Tang, *Coord. Chem. Rev.*, 2021, **431**, 213666.
26 K. S. Kumar and M. Ruben, *Coord. Chem. Rev.*, 2017, **346**, 176–205.
27 T. Charytanowicz, J. Wang, H. Tokoro, K. Tran, F. Renz, S. I. Ohkoshi, S. Chorazy and B. Sieklucka, *Angew. Chem., Int. Ed.*, 2025, **137**, e202419242.
28 P. Gütlich and H. A. Goodwin, *Spin Crossover in Transition Metal Compounds I*, 2004, pp. 1–47.
29 N. Amin, S. Said, M. Salleh, A. Afifi, N. Ibrahim, M. Hasnan, M. Tahir and N. Hashim, *Inorg. Chim. Acta*, 2023, **544**, 121168.
30 K. S. Kumar and M. Ruben, *Angew. Chem., Int. Ed.*, 2021, **60**, 7502–7521.
31 H. Li and H. Peng, *Curr. Opin. Colloid Interface Sci.*, 2018, **35**, 9–16.
32 G. Molnár, L. Salmon, W. Nicolazzi, F. Terki and A. Bousseksou, *J. Mater. Chem. C*, 2014, **2**, 1360–1366.
33 D. J. Harding, P. Harding and W. Phonsri, *Coord. Chem. Rev.*, 2016, **313**, 38–61.
34 Y. Garcia, J. Moscovici, A. Michalowicz, V. Ksenofontov, G. Levchenko, G. Bravic, D. Chasseau and P. Gütlich, *Chem. – Eur. J.*, 2002, **8**, 4992–5000.
35 H. Banerjee, M. Kumar and T. Saha-Dasgupta, *Phys. Rev. B*, 2014, **90**, 174433.
36 R. W. Hogue, S. Singh and S. Brooker, *Chem. Soc. Rev.*, 2018, **47**, 7303–7338.
37 O. Kahn, J. Kröber and C. Jay, *Adv. Mater.*, 1992, **4**, 718–728.
38 J. Kröber, E. Codjovi, O. Kahn, F. Groliere and C. Jay, *J. Am. Chem. Soc.*, 1993, **115**, 9810–9811.
39 O. Kahn, L. Sommier and E. Codjovi, *Chem. Mater.*, 1997, **9**, 3199–3205.
40 P. J. van Koningsbruggen, Y. Garcia, E. Codjovi, R. Lapouyade, O. Kahn, L. Fournes and L. Rabardel, *J. Mater. Chem.*, 1997, **7**, 2069–2075.
41 Y. Garcia, V. Niel, M. C. Muñoz and J. A. Real, *Top. Curr. Chem.*, 2004, **233**, 229–257.
42 Y. Garcia, *Adv. Inorg. Chem.*, 2020, **76**, 121–153.
43 Z. Wang, L. P. Zhou, L. X. Cai, C. B. Tian and Q.-F. Sun, *Nano Res.*, 2021, **14**, 398–403.
44 A. Grosjean, N. Daro, B. Kauffmann, A. Kaiba, J.-F. Létard and P. Guionneau, *Chem. Commun.*, 2011, **47**, 12382–12384.
45 H. S. Scott, R. W. Staniland and P. E. Kruger, *Coord. Chem. Rev.*, 2018, **362**, 24–43.
46 D. Tesfaye, W. Linert, M. Gebrezgiabher, Y. Bayeh, F. Elemo, T. Sani, N. Kalarikkal and M. Thomas, *Molecules*, 2023, **28**, 1012.
47 C. J. Cox, J. Hale, P. Molinska and J. E. Lewis, *Chem. Soc. Rev.*, 2024, **53**, 10380–10408.
48 D. Zhang, T. K. Ronson and J. R. Nitschke, *Acc. Chem. Res.*, 2018, **51**, 2423–2436.
49 T. Paschelke, E. Trumpf, D. Grantz, M. Pankau, N. Grocholski, C. Näther, F. D. Sönnichsen and A. J. McConnell, *Dalton Trans.*, 2023, **52**, 12789–12795.
50 Z. Shao, Y.-S. Meng, Y.-Y. Zhu and T. Liu, *Dalton Trans.*, 2025, **54**, 12432–12442.
51 F. Yin, J. Yang, L.-P. Zhou, X. Meng, C.-B. Tian and Q.-F. Sun, *J. Am. Chem. Soc.*, 2024, **146**, 7811–7821.
52 N. Struch, C. Bannwarth, T. K. Ronson, Y. Lorenz, B. Mienert, N. Wagner, M. Engeser, E. Bill, R. Puttreddy and K. Rissanen, *Angew. Chem., Int. Ed.*, 2017, **56**, 4930–4935.
53 W. Li, L. Sun, C. Liu, A. Rotaru, K. Robeyns, M. L. Singleton and Y. Garcia, *J. Mater. Chem. C*, 2022, **10**, 9216–9221.
54 M. B. Duriska, S. M. Neville, B. Moubaraki, J. D. Cashion, G. J. Halder, K. W. Chapman, C. Balde, J. F. Létard, K. S. Murray and C. J. Kepert, *Angew. Chem., Int. Ed.*, 2009, **121**, 2587–2590.
55 M. B. Duriska, S. M. Neville, B. Moubaraki, K. S. Murray, C. Balde, J. F. Létard, C. J. Kepert and S. R. Batten, *ChemPlusChem*, 2012, **77**, 616–623.
56 N. Struch, C. Bannwarth, T. K. Ronson, Y. Lorenz, B. Mienert, N. Wagner, M. Engeser, E. Bill, R. Puttreddy, K. Rissanen, J. Beck, S. Grimme, J. R. Nitschke and A. Lützen, *Angew. Chem., Int. Ed.*, 2017, **56**, 4930–4935.
57 M. Hardy, J. Tessarolo, J. J. Holstein, N. Struch, N. Wagner, R. Weisbarth, M. Engeser, J. Beck, S. Horiuchi and G. H. Clever, *Angew. Chem., Int. Ed.*, 2021, **60**, 22562–22569.
58 I. C. Berdiell, T. Hochdörffer, C. Desplanches, R. Kulmaczewski, N. Shahid, J. A. Wolny, S. L. Warriner, O. Cespedes, V. Schünemann and G. Chastanet, *J. Am. Chem. Soc.*, 2019, **141**, 18759–18770.
59 H.-S. Lu, W.-K. Han, X. Yan, Y.-X. Xu, H.-X. Zhang, T. Li, Y. Gong, Q.-T. Hu and Z.-G. Gu, *Dalton Trans.*, 2020, **49**, 4220–4224.
60 H. Min, A. R. Craze, M. J. Wallis, R. Tokunaga, T. Taira, Y. Hirai, M. M. Bhadbhade, D. J. Fanna, C. E. Marjo and S. Hayami, *Chem. – Eur. J.*, 2023, **29**, e202203742.
61 Y. R. Hristova, M. M. Smulders, J. K. Clegg, B. Breiner and J. R. Nitschke, *Chem. Sci.*, 2011, **2**, 638–641.
62 E. G. Percástegui, J. Mosquera and J. R. Nitschke, *Angew. Chem., Int. Ed.*, 2017, **129**, 9264–9268.
63 H. S. Scott, R. W. Staniland and P. E. Kruger, *Coord. Chem. Rev.*, 2018, **362**, 24–43.
64 A. J. McConnell, *Chem. Soc. Rev.*, 2022, **51**, 2957–2971.
65 E. Raee, Y. Yang and T. Liu, *Giant*, 2021, **5**, 100050.
66 Z.-H. Luo, Y.-L. Zhu, X.-Y. Ran, A.-X. Ma, Y. Zhang, H.-M. Zhou, B.-J. Wang, J.-H. Zhang, S.-M. Xie and L.-M. Yuan, *Talanta*, 2024, **277**, 126388.

67 J. R. Nitschke, *Acc. Chem. Res.*, 2007, **40**, 103–112.
68 A. M. Castilla, W. J. Ramsay and J. R. Nitschke, *Acc. Chem. Res.*, 2014, **47**, 2063–2073.
69 T. K. Ronson, S. Zarra, S. P. Black and J. R. Nitschke, *Chem. Commun.*, 2013, **49**, 2476–2490.
70 A.-M. Yang, X.-H. Qin, H.-Y. Li, D. Yao and F.-P. Huang, *CrystEngComm*, 2025, **27**, 4634–4641.
71 A. J. McConnell, *Supramol. Chem.*, 2018, **30**, 858–868.
72 S.-L. Yang, X. Zhang, Q. Wang, C. Wu, H. Liu, D. Jiang, R. Lavendomme, D. Zhang and E.-Q. Gao, *JACS Au*, 2023, **3**, 2183–2191.
73 Y. Sunatsuki, R. Kawamoto, K. Fujita, H. Maruyama, T. Suzuki, H. Ishida, M. Kojima, S. Iijima and N. Matsumoto, *Coord. Chem. Rev.*, 2010, **254**, 1871–1881.
74 K. Fujita, R. Kawamoto, R. Tsubouchi, Y. Sunatsuki, M. Kojima, S. Iijima and N. Matsumoto, *Chem. Lett.*, 2007, **36**, 1284–1285.
75 N. Bibi, E. G. R. de Arruda, A. Domingo, A. A. Oliveira, C. Galuppo, Q. M. Phung, N. M. Orra, F. Beron, A. Paesano Jr and K. Pierloot, *Inorg. Chem.*, 2018, **57**, 14603–14616.
76 A. Ferguson, M. A. Squire, D. Siretanu, D. Mitcov, C. Mathoniere, R. Clérac and P. E. Kruger, *Chem. Commun.*, 2013, **49**, 1597–1599.
77 R. A. Bilbeisi, S. Zarra, H. L. Feltham, G. N. Jameson, J. K. Clegg, S. Brooker and J. R. Nitschke, *Chem. – Eur. J.*, 2013, **19**, 8058–8062.
78 L. Li, N. Saigo, Y. Zhang, D. J. Fanna, N. D. Shepherd, J. K. Clegg, R. Zheng, S. Hayami, L. F. Lindoy and J. R. Aldrich-Wright, *J. Mater. Chem. C*, 2015, **3**, 7878–7882.
79 D.-H. Ren, D. Qiu, C.-Y. Pang, Z. Li and Z.-G. Gu, *Chem. Commun.*, 2015, **51**, 788–791.
80 F.-L. Zhang, J.-Q. Chen, L.-F. Qin, L. Tian, Z. Li, X. Ren and Z.-G. Gu, *Chem. Commun.*, 2016, **52**, 4796–4799.
81 L. Li, A. R. Craze, O. Mustonen, H. Zenno, J. J. Whittaker, S. Hayami, L. F. Lindoy, C. E. Marjo, J. K. Clegg, J. R. Aldrich-Wright and F. Li, *Dalton Trans.*, 2019, **48**, 9935–9938.
82 H.-X. Zhang, X. Yan, Y.-X. Chen, S.-H. Zhang, T. Li, W.-K. Han, L.-Y. Bao, R. Shen and Z.-G. Gu, *Chem. Commun.*, 2019, **55**, 1120–1123.
83 W.-K. Han, H.-X. Zhang, Y. Wang, W. Liu, X. Yan, T. Li and Z.-G. Gu, *Chem. Commun.*, 2018, **54**, 12646–12649.
84 T. Tanaka, Y. Sunatsuki and T. Suzuki, *Inorg. Chim. Acta*, 2020, **502**, 119373.
85 W. Li, C. Liu, J. Kfoury, J. Oláh, K. Robeyns, M. L. Singleton, S. Demeshko, F. Meyer and Y. Garcia, *Chem. Commun.*, 2022, **58**, 11653–11656.
86 W. Li, X. Li, K. Robeyns, M. Wolff, J. Kfoury, J. Oláh, R. Herchel, S. Demeshko, F. Meyer and Y. Garcia, *Dalton Trans.*, 2024, **53**, 1449–1459.
87 A. Gupta, A. Patra and S. Konar, *Eur. J. Inorg. Chem.*, 2025, **00**, e202500046.
88 J. B. Maglic and R. Lavendomme, *J. Appl. Crystallogr.*, 2022, **55**, 1033–1044.
89 C. M. Hong, R. G. Bergman, K. N. Raymond and F. D. Toste, *Acc. Chem. Res.*, 2018, **51**, 2447–2455.
90 P. Mal, D. Schultz, K. Beyeh, K. Rissanen and J. R. Nitschke, *Angew. Chem., Int. Ed.*, 2008, **47**, 8297–8301.
91 W. Li, A. Rotaru, M. Wolff, S. Demeshko, F. Meyer and Y. Garcia, *J. Mater. Chem. C*, 2023, **11**, 11175–11184.

